

4000  
IX, 53

UNIVERSITY OF HAWAII LIBRARY  
ON THE MODELING OF THE HYDRODYNAMIC FORCE ACTING ON A  
SPHERICAL PARTICLE

A THESIS SUBMITTED TO THE GRADUATE DIVISION OF THE  
UNIVERSITY OF HAWAII IN PARTIAL FULFILLMENT OF THE  
REQUIREMENTS FOR THE DEGREE OF

MASTER OF SCIENCE  
IN  
MECHANICAL ENGINEERING

AUGUST 2005

By  
Hugo T. C. Pedro

Thesis Committee:

Marcelo H. Kobayashi, Chairperson  
Janet M. Becker  
Carlos F. M. Coimbra

# Acknowledgements

I would like to express my sincere gratitude to Prof. Marcelo Kobayashi, my advisor, for his guidance and constant support during this research. I am also thankful to Prof. Carlos Coimbra for all the useful suggestions.

I should also mention José Pereira and Prof. José Carlos Pereira from the Technical University of Lisbon for their support in the beginning of my research.

Also, I am grateful to Prof. Janet Becker for all suggestions to improve this thesis.

Finally, I am grateful to my family for their patience and love. Without them this work would never have come into existence.

# Abstract

A new model of the hydrodynamic force acting on a particle under an oscillating viscous fluid flow, at finite Reynolds and Strouhal numbers in the range of 0.01 to 25 is developed. This drag model is based on the novel concept of variable-order calculus, where the order of derivative can vary with the dynamics of the flow.

A numerical simulation, based on a fourth-order compact scheme in space and a implicit third-order time-marching scheme has been used to compute the time-dependent, axisymmetric viscous flow past the rigid sphere. The solution is used to determine the appropriate differential operator (constant or variable) in the drag model for the several cases simulated. Also, it is determined: (i) the region of validity of the creeping flow equation for an oscillatory flow, (ii) the region where the order of the derivative is fractional, but constant and (iii) the region where the strong non-linearity of the flow requires a variable-order derivative to account for the increased complexity of the drag force behavior.

The proposed drag model is able to accurately predict the hydrodynamic force acting on the sphere within the parameter range investigated. For moderate values of the Reynolds numbers, the constant-order model provides an accurate description of the drag. Increasing the Reynolds number or decreasing the product of the Reynolds and Strouhal numbers leads to non-linear effects, which require a variable-order differential operator to model accurately the history effects on the drag.

# Table of Contents

Acknowledgements . . . . .	iii
Abstract . . . . .	iv
List of Tables . . . . .	vii
List of Figures . . . . .	viii
Chapter 1: Introduction . . . . .	1
1.1 Background . . . . .	2
1.2 Objectives and contributions of the present work . . . . .	5
Chapter 2: Modeling of the hydrodynamic force . . . . .	6
2.1 Introduction . . . . .	6
2.2 The hydrodynamic force acting on the sphere . . . . .	7
2.3 Mathematical description of the FO and VO derivatives . . . . .	10
2.4 Least squares method . . . . .	12
Chapter 3: Numerical Methods . . . . .	16
3.1 Introduction . . . . .	16
3.1.1 Governing equations . . . . .	17
3.1.2 Boundary conditions . . . . .	18
3.2 Spatial discretization . . . . .	20
3.2.1 Internal nodes . . . . .	20
3.2.2 Boundary nodes . . . . .	22
3.3 Time discretization . . . . .	23
3.4 The Solver: Newton-Krylov-multigrid matrix free method . . . . .	26
Chapter 4: Results and discussion . . . . .	29

4.1	Validation of the numerical code . . . . .	29
4.1.1	Order of accuracy . . . . .	29
4.1.2	Sphere drag validation . . . . .	31
4.2	Validation of the least-squares method . . . . .	35
4.3	Modeling of the hydrodynamic force . . . . .	36
4.3.1	Fractional-Order . . . . .	37
4.3.2	Variable-Order . . . . .	42
Chapter 5: Conclusions and Future Work . . . . .		48
Bibliography . . . . .		51

# List of Tables

3.1	Time discretization coefficients $a_j$ and $b_j$ . . . . .	24
4.1	Error evolution ( $L_2$ norm) with the grid - fourth-order accuracy. . . .	30
4.2	Error evolution ( $L_2$ norm) with the grid - second-order accuracy. . . .	31

# List of Figures

2.1	VO and FO of $x(t) = t$ . The thick black curve is the VO derivative of order $t$ . The other curves are the 1/4 (dash), 1/2 (dot), 3/4 (dash-dot) FO derivatives derivatives of $x(t) = t$ . . . . .	12
3.1	Geometry of the numerical domain . . . . .	19
3.2	Stability region (to the right and below the lines) for each temporal discretization schemes. Second-order spatial approximation with: fourth-order in time (left), third-order in time (right). . . . .	25
3.3	Stability region (to the right and below the lines) for each temporal discretization schemes. Fourth-order compact spatial approximation with: fourth-order in time (left), third-order in time (right). . . . .	26
4.1	Drag experienced by the sphere for a steady flow as function of $Re$ . Line: numerical solution. Dots: experimental data. . . . .	32
4.2	Stream lines for several Reynolds. (a) $Re = 1.0$ , (b) $Re = 10$ , (c) $Re = 40$ , (d) $Re = 50$ . . . . .	33
4.3	Multigrid effect on the convergence history . . . . .	33
4.4	Drag experienced by the sphere for an unsteady flow with $ReSl = 1$ and $Re = 0.01$ (left) and and $Re = 0.1$ (right). Line: analytic solution. Dots: numerical data. . . . .	34
4.5	Drag experienced by the sphere for an unsteady flow with $ReSl = 2$ and $Re = 0.01$ (left) and and $Re = 0.1$ (right). Line: analytic solution. Dots: numerical data. . . . .	35

4.6	Verification of our optimization method. Left: FO-derivative order function of $ReSl$ . Right: FO-derivative coefficient function of $ReSl$ . Line: analytical result. Dots: numerical result. . . . .	36
4.7	Drag $q$ -order as a function of $ReSl$ and $Re$ . . . . .	37
4.8	Drag $F$ -coefficient as a function of $ReSl$ and $Re$ . . . . .	38
4.9	Region of validity of creeping flow equation (white), FO drag model (light grey + white), and VO drag model (dark grey) . . . . .	40
4.10	Sphere drag for $Re = 20$ , $ReSl = 10$ ( $\bullet$ in the figure 4.9). Line: creeping flow equation (2.2.3), dots: numerical solution. . . . .	41
4.11	Sphere drag for $Re = 20$ , $ReSl = 1$ ( $\star$ in the figure 4.9). Dash line: creeping flow equation (2.2.3), solid line: FO equation (2.2.6) with $q = 0.365$ , $F = 1.94$ , dots: numerical solution. . . . .	41
4.12	Sphere drag for $Re = 20$ , $ReSl = 0.01$ ( $\blacktriangle$ in the figure 4.9). Solid line: FO equation (2.2.6) with $q = 0.021$ , $F = 2.47$ , dots: numerical solution. . . . .	42
4.13	Snapshots of the flow at several instants $t = \phi/9$ with $\phi = \{2\pi/16, 6\pi/16, 8\pi/16, 10\pi/16, 14\pi/16\}$ for the oscillatory background flow $u(t) = \sin(9t)$ , for $Re = 0.01$ , $ReSl = 0.01$ . . . . .	43
4.14	Snapshots of the flow at several instants $t = \phi/9$ with $\phi = \{3\pi/16, 5\pi/16, 7\pi/16, 9\pi/16, 11\pi/16, 13\pi/16, 15\pi/16\}$ for the oscillatory background flow $u(t) = \sin(9t)$ , for $Re = 20$ , $ReSl = 0.01$ . . . . .	43
4.15	Coefficients $a_1, a_2, a_3$ and $F$ for $ReSl=0.01$ . . . . .	45
4.16	Sphere drag for $ReSl = 0.01$ using the VO derivative in the drag model for several $Re$ : (a) $Re = 20$ , (b) $Re = 10$ , (d) $Re = 5$ and (c) $Re = 2$ . The drag is computed with (2.2.6) and $q$ is given by (4.3.1) . . . . .	46
4.17	Order of the derivative $q$ as a function of $t$ and $Re$ for $ReSl = 0.01$ . $q$ is given by (4.3.1) for $Re > 1$ , otherwise $q$ is the constant value determined with the FO model shown in figure 4.7. . . . .	47

# Chapter 1

## Introduction

The knowledge of the drag force on a particle is required for many applications such as particle sedimentation, particles in colloidal suspension, particle image velocimetry (PIV), and droplet combustion. Only with the correct knowledge of this force may we predict the motion of the particle. Closed-form solutions for the hydrodynamic force exist only in the limit of infinitesimal Reynolds numbers (e.g. Stokes [26], Basset [2]). Many empirical corrections extend the classical solution to finite  $Re$ , but their validity is limited.

In this work, we use the novel concept of variable-order differential operators to model the hydrodynamic force acting on the particle for an oscillating flow at moderate Reynolds and Strouhal numbers, defined as  $Re = U_c a / \nu_f$  and  $Sl = a / (U_c t_c)$  where  $U_c$  is a characteristic flow velocity,  $\nu_f$  is the kinematic fluid viscosity,  $a$  is a characteristic particle dimension and  $t_c$  is a characteristic time. In this study, we consider Reynolds numbers that correspond only to laminar axisymmetric flow past the particle.

As the order of the derivative may be related to the memory effect of the flow on the particle, the proposed approach provides more physical insight than previous

models. This characteristic makes the model presented here valuable not only from a quantitative perspective, but also from a dynamical point of view.

This thesis is organized in the following manner: in the first chapter we review previous work concerning the hydrodynamic force acting on a particle. In chapter two, the new approach proposed here is presented. This concept demands some less well known mathematical tools which are presented briefly in the beginning of the chapter. Here, we also present the method used to determine the differential operator that models the drag force on the particle. In the third chapter, we present a new numerical method to calculate the flow field around the particle and the force acting on it. In particular, we discuss the space and time discretizations and the numerical continuation method. Chapter four addresses the verification and validation of the numerical methods introduced in previous chapters. Several test cases are run to assess the accuracy of the numerical methods. Moreover we present and discuss the results of our proposed model, namely the determination of the FO and VO operators to model the drag force. Finally, in the chapter five we summarize the main conclusions from the present work and suggest directions for future work.

## 1.1 Background

The unsteady hydrodynamic force or drag acting on a sphere, due to an oscillating flow is a classical problem in fluid mechanics. Several models have been developed by the many researchers who have studied this problem.

The first studies date back to the nineteenth century and rely on the assumption of infinitesimal Reynolds number to linearize the Navier-Stokes equation by neglecting the convection term. This procedure returns the Stokes or creeping flow equation,

which has been solved analytically by different researchers (Stokes [26], Basset [2], Boussinesq [3], and Oseen [20]), giving the following equation for the force acting on a moving particle in an stagnant fluid

$$\begin{aligned} \mathbf{D} = & 6\pi a\mu_f \mathbf{V} + \frac{1}{2}m_f \frac{d\mathbf{V}}{dt} + \\ & + 6a^2 \sqrt{\pi\mu_f\rho_f} \int_0^t (t-\tau)^{-\frac{1}{2}} \frac{d\mathbf{V}}{d\tau} d\tau + (m_p - m_f)\mathbf{g} \end{aligned} \quad (1.1.1)$$

where  $\mathbf{V}$  is the sphere velocity vector,  $a$  is the sphere radius,  $m_f$  is the mass of fluid displaced by the sphere,  $m_p$  is the mass of the particle,  $\mathbf{g}$  is the gravitational acceleration vector, and  $\mu_f$  is dynamic viscosity. In this work bold symbols are reserved to vectors and matrices.

The first term in (1.1.1) is the steady Stokes drag, the second is the virtual mass force and third is the Basset history drag. The last term is the buoyancy force which is not taken into account in this work since the sphere is fixed.

More recently Maxey and Riley [15] rederived an equation that generalizes (1.1.1) when the fluid is in motion and/or not uniform. Their analysis yields

$$\begin{aligned} \mathbf{D} = & 6\pi a\mu_f (\mathbf{U} - \mathbf{V}) + \frac{1}{2}m_f \frac{d(\mathbf{U} - \mathbf{V})}{dt} + m_f \frac{D\mathbf{U}}{Dt} + \\ & + 6a^2 \sqrt{\pi\mu_f\rho_f} \int_0^t (t-\tau)^{-\frac{1}{2}} \frac{d(\mathbf{U} - \mathbf{V})}{d\tau} d\tau \end{aligned} \quad (1.1.2)$$

where  $\mathbf{U}$  is the fluid velocity.

Apart from these analytical works, experimental and numerical results have resulted in empirical expressions for the drag force that extend the previous results to noncreeping flow. Odar and Hamilton [19] used the creeping flow equation (1.1.2) and multiplied each term by a correction coefficient. The unknown coefficients were then found by matching this corrected analytical result with experimental data.

More recent work (Mei, Lawrence and Adrian [18] and Chang and Maxey [5], [6]) has shown that the added-mass term for finite Reynolds numbers flows is the same as predicted by Stokes equation which means that the correction coefficient for this term is unity. However, as we would expect, the other two terms are not correct when the Reynolds number is finite. Moreover it has been demonstrated that the kernel in the Basset term does not decay with  $(t - \tau)^{-1/2}$  when  $Re$  increases. Mei [16] and Mei and Adrian [17] used a matched asymptotic expansion for small Reynolds and low frequency oscillatory motion combined with numerical results at higher  $Re$  numbers to propose the equation

$$\begin{aligned} \mathbf{D} = & -\frac{1}{2}C_{Dstd}\pi a^2\rho_f(\mathbf{U} - \mathbf{V})|\mathbf{U} - \mathbf{V}| - \frac{1}{2}m_f\left(\frac{D\mathbf{U}}{Dt} - \frac{d\mathbf{V}}{dt}\right) - m_f\frac{D\mathbf{U}}{Dt} + \\ & + 6\pi\mu_f a \int_{-\infty}^t K(t - \tau, \tau) \frac{d(\mathbf{U} - \mathbf{V})}{d\tau} d\tau \end{aligned} \quad (1.1.3)$$

where  $C_{Dstd}$  is the drag coefficient from the standard steady drag curve. The integral kernel is such that results given by this equation match the numerical simulations.

By this method they obtained the following kernel

$$K(t - \tau, \tau) = \left\{ \left[ \frac{\pi(t - \tau)\nu_f}{a^2} \right]^{1/4} + \left[ \frac{\pi|U(\tau) - V(\tau)|^3}{2a\nu_f f_H^3(Re_p)} (t - \tau)^2 \right]^{1/2} \right\}^{-2} \quad (1.1.4)$$

where  $f_H(Re_p) = 0.75 + 0.105Re_p(\tau)$ , and  $Re_p$  is the particle Reynolds number defined as  $Re_p = |U(\tau) - V(\tau)|a/\nu_f$ .

Kim, Elghobashi and Sirignano [9] used the same approach to propose a kernel that approximates the numerical results over the range of Reynolds 1 to 75. Their kernel is even more complicated and relies on several empirical coefficients. A common feature of the memory integrals developed by the researchers is the fact the all depend on the instantaneous Reynolds number,  $Re_p$ , in such way that for small  $Re_p$  the original Basset term is recovered (the first term in the kernel).

## 1.2 Objectives and contributions of the present work

All previous attempts to model the hydrodynamic drag force for flows with finite Reynolds numbers suffer from a lack of physical meaning since the kernel has no obvious dynamical interpretation. So the main goal of this work is to model the hydrodynamic force for finite Reynolds numbers using the constant fractional-order (FO) differential calculus and the variable-order (VO) differential calculus which will provided physical insight to this problem.

Here, starting from the analytical solution for Stokes flow, we extend this solution to finite Reynolds numbers by considering first a FO differential operator and then a VO differential operator in the drag force model. The limits of validity of the several models are studied and clarified. This is an important contribution since, to the best of our knowledge, these limits are not known.

Besides the contribution to the knowledge of the hydrodynamic drag force, we also developed a new, high order, implicit numerical method with very good stability properties to compute the unsteady flow around the sphere.

# Chapter 2

## Modeling of the hydrodynamic force

In this chapter we introduce the modeling of the hydrodynamic drag force with the FO and VO differential operators. Also, we introduce the mathematical definition of the differential operators as well as the methodology used to determine these operators.

### 2.1 Introduction

In the recent years, Coimbra and Rangel [8] have shown that the history term in the unsteady creeping flow equation (1.1.2) is in fact the one-half fractional-order derivative of the relative velocity. Bearing this in mind, we propose a new approach to model the drag for higher Reynolds numbers. Our goal is to express the particle drag as the VO derivative of the relative velocity between the fluid and the particle. This option is justified by the fact that VO derivatives have a physical interpretation that the previous approaches lack. Also the VO model emerges in this work as the natural generalization of the FO differential operator that appears as the Basset term in the classical creeping flow equation.

In the classical equation of the unsteady Stokes flow, the total force acting on the sphere includes contributions that are proportional to the relative velocity (Stokes drag), the half-derivative of the relative velocity (the Basset drag), and the relative acceleration (the virtual mass force). These forces may be identified as the the zero, half and first-order derivatives of the particle velocity, respectively.

When we depart from the Stokes equation by increasing the Reynolds number (larger particle or higher velocities or less viscous fluid) the order of the derivatives is altered. In the beginning for small but finite Reynolds numbers the order of the derivative still remains constant but eventually, as  $Re$  increases, it becomes dependent of the particle Reynolds number  $Re_p$ , and therefore variable in time. At this point the dynamics may be modeled with a VO differential operator instead of a Constant-Order (CO) differential operator. So we consider the creeping flow equation derived by Maxey and Riley (1.1.2) and seek to extend it to finite Reynolds numbers.

## 2.2 The hydrodynamic force acting on the sphere

Let us specify the creeping flow equation for the case considered here. In the present work the particle is assumed to be fixed, hence  $\mathbf{V} = 0$ . Moreover, the fluid velocity is sinusoidal in time but uniform in space  $\mathbf{U}(t) = U_0 \sin(\omega t) \mathbf{e}_x$  and the substantial derivative in equation (1.1.2) reduces to the time derivative  $d\mathbf{U}/dt$ . Therefore the vectorial equation (1.1.2) is simplified to one equation in the flow direction

$$D = 6\pi a\mu_f U + \frac{3}{2}m_f \frac{dU}{dt} + 6a^2\sqrt{\pi\mu_f\rho_f} \int_0^t (t - \tau)^{-\frac{1}{2}} \frac{dU}{d\tau} d\tau \quad (2.2.1)$$

This equation is then made dimensionless using the following characteristic dimensions

$$L_c = a, t_c = \frac{9}{\omega}, U_c = U_0 \quad (2.2.2)$$

where  $a$  is the sphere radius,  $t_c$  is proportional to the flow period (the 9 is a geometrical factor for the sphere) and  $U_0$  is the velocity amplitude of the background flow. Therefore, the nondimensional drag force for the creeping flow ( $cf$ ) is given by

$$f_{cf} = u + \frac{ReSl}{3} \frac{du}{dt} + \frac{\sqrt{ReSl}}{\sqrt{\pi}} \int_0^t (t - \tau)^{-\frac{1}{2}} \frac{du}{d\tau} d\tau \quad (2.2.3)$$

where the non-dimensional quantities

$$Re = \frac{U_0 a}{\nu_f}, \quad Sl = \frac{a\omega}{9U_0} \quad (2.2.4)$$

are the Reynolds number and the Strouhal number, respectively. Here we work with the nondimensional numbers  $ReSl$  and  $Re$  instead of  $Re$  and  $Sl$  because  $ReSl = a^2\omega/(9\nu_f)$  is the governing parameter for creeping flow, as equation (2.2.3) shows.

The latter equation may be written using an equivalent notation

$$f_{cf} = \mathcal{D}^0 u + \frac{ReSl}{3} \mathcal{D}^1 u + \sqrt{ReSl} \mathcal{D}^{\frac{1}{2}} u \quad (2.2.5)$$

In this work, we reserve uppercase symbols to indicate dimensional dependent variables (with obvious exceptions, such as  $Re$  and  $Sl$ ). We refer to the corresponding dimensionless quantities by lowercase symbols. The independent variables are always represented by lowercase symbols, whether or not they are dimensionless is determined by the dependent variables in the equation.

As mentioned above, the creeping flow drag is governed by  $ReSl$ . When extending the result to finite  $Re$  is obvious the drag force will also depend on  $Re$ . So we seek

a model of the total hydrodynamic force acting on the spherical particle for finite Reynolds number as

$$f_T \equiv F(Re, ReSl, u)\mathcal{D}^{q(Re, ReSl, u)}u + \frac{ReSl}{3}\mathcal{D}^1u. \quad (2.2.6)$$

Here the virtual mass term is left unchanged because, as stated before, it is found to be valid for noncreeping flow. The other two contributions are combined in one term since both are viscous forces. This procedure seems natural and can be better understood when we consider a potential inviscid flow ( $Re \rightarrow \infty$ ). In that case the virtual mass term contributes in the same manner to the drag force whereas the other two have no contribution since there is no viscosity. This means that the the virtual mass term is valid for the all range of  $Re$  numbers.

Ideally,  $F$  and  $q$  should be derived from the Navier-Stokes equations, but since no analytical solution of these equations is currently available, as a first step to understand the effects of the convective inertia on  $F$  and  $q$ , we will determine approximate expressions for  $F$  and  $q$  in the range of  $Re \times ReSl = [0.01, 25] \times [0.01, 25]$ . The upper limit is dictated by the appearance of asymmetries in the wake which make the flow tridimensional. Increasing  $Re$  further leads to a non-axisymmetric wake and eventually to turbulence.

Our strategy is to obtain the force acting on the particle numerically and then use that data to determine the differential operator. We use a high-order numerical method to obtain the numerical flow field over the sphere, from which we compute the drag acting on the sphere by integrating the normal and shear stress around the particle. Using that value we determine  $F$  and  $q$  in the equation (2.2.6) such that it matches the numerical data.

This approach leads to a model of the hydrodynamic force where all terms are

derivatives (FO or VO) of the relative velocity. The order of the derivative can be related to memory effects and viscoelastic behavior, phenomena already familiar in fluid mechanics. In fact, when  $q \rightarrow 1$  the derivative in equation (2.2.6) for the hydrodynamic force depends only on the instantaneous acceleration and not on the velocity itself nor on any velocity history. So, as  $q \rightarrow 1$  the fractional derivative  $\mathcal{D}^q \rightarrow \mathcal{D}^1$  and any memory effect is lost. On the other hand, as  $q \rightarrow 0$ , we have  $\mathcal{D}^q \rightarrow 1$  and the memory effect is maximum. So, for the creeping flow equation the Basset term accounts for a perfectly symmetrical memory, midway between  $q = 0$  and  $q = 1$ . In summary the VO derivative represents the memory effect at each instant to which it is applied. The FO derivative has the same interpretation but without varying in time.

## 2.3 Mathematical description of the FO and VO derivatives

The FO calculus is an old topic in Mathematics but until the end of last century it was ignored as a modeling tool. In the past decade, however, many new practical applications of Fractional Calculus have been studied and reported ([22], [14] and [8]). One of the most well known problems that is observed experimentally is the viscoelastic damping that varies with the  $1/2$  derivative of the displacement. Also, in the field of rheology is found that the stress-strain relationship of materials often lies in between an elastic solid and a purely viscous fluid. This includes the behavior of suspensions and polymers in general. The dynamics of these materials exhibit memory, a characteristic that is identified with non-integer order formulations as we

have seen, so the FO and VO tools seem to be particularly suited to model such behaviors.

There is more than one way to define the FO differential operator, namely Caputo's definition and the Riemann-Liouville definition. Following the analysis of Coimbra [7] we adopt Caputo's definition due to its straightforwardness and easier physical interpretation. Following Caputo's the FO derivative is

$$\mathcal{D}^q x(t) = \frac{1}{\Gamma(n-q)} \int_{0^-}^t (t-\tau)^{n-q-1} x^{(n)}(\tau) d\tau, \quad n-1 < q < n \quad (2.3.1)$$

with  $n$  integer.

The extension from constant-order to variable-order differentials is based on the Caputo's FO definition as was suggested by Coimbra [7]. It can be shown that the variable-order derivative, specified for  $0 < q(t) < 1$ , of a given function  $x(t)$  is

$$\mathcal{D}^{q(t)} x(t) = \frac{1}{\Gamma(1-q(t))} \int_{0^+}^t (t-\tau)^{-q(t)} x'(\tau) d\tau + \frac{(x_{0^+} - x_{0^-}) t^{q(t)}}{\Gamma(1-q(t))} \quad (2.3.2)$$

We choose this definition following the reasons invoked in Coimbra and also in Soon *et al* [25], which are basically the ones referred before for the FO differential operator: straightforwardness and easier physical interpretation. In fact, the differential operator (2.3.2) has a clear physical meaning which the alternatives do not possess: for any particular time  $t$ , the VO differential operator specified above returns the  $q(t)^{th}$  order derivative of the function  $x(t)$ . This way the operator  $\mathcal{D}^t t$  returns the  $0^{th}$  derivative of  $t$  at  $t = 0$ , the half-derivative at  $t = 1/2$  and the first derivative at  $t = 1$  which means that the FO differential operator (2.3.1) is a particular case of the VO operator (2.3.2). This behavior is shown in figure 2.1 for the FO derivative  $1/4, 1/2$  and  $3/4$  of the function  $x(t) = t$ .

The restriction  $0 < q(t) < 1$  is extended also to the FO differential operator (2.3.1)

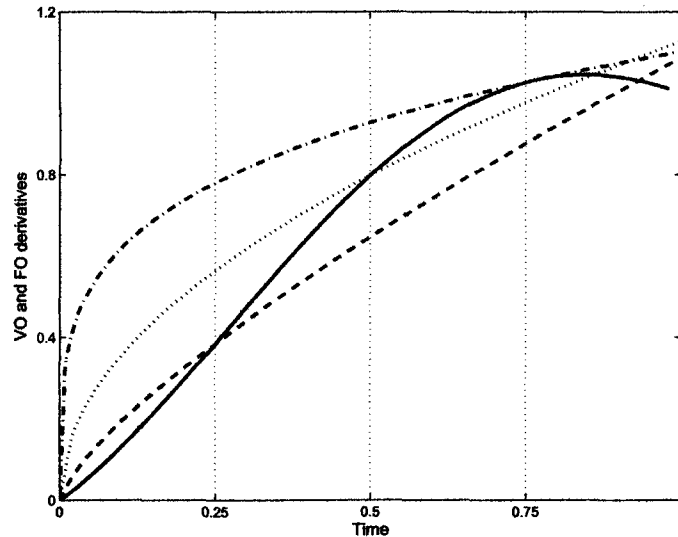


Figure 2.1: VO and FO of  $x(t) = t$ . The thick black curve is the VO derivative of order  $t$ . The other curves are the  $1/4$  (dash),  $1/2$  (dot),  $3/4$  (dash-dot) FO derivatives derivatives of  $x(t) = t$

yielding

$$\mathcal{D}^q x(t) = \frac{1}{\Gamma(1-q)} \int_{0^-}^t (t-\tau)^{-q} x'(\tau) d\tau \quad (2.3.3)$$

This condition will not constrain our results since, in fact, we expect  $q$  to vary between 0 and  $1/2$ : for low frequency flows the Stokes drag dominates the force consequently the order of the derivative must approach 0, whereas for high frequencies the memory effect grows in importance and  $q$  is expected to approach  $1/2$ .

## 2.4 Least squares method

As mentioned above  $q$  and  $F$  are determined numerically by assuring the best fit of the new model for the hydrodynamic force (2.2.6) to the reference numerical results.

In this section we describe the least-squares algorithm used to determine  $q$  and  $F$ .

The order of the derivative,  $q$ , and the coefficient,  $F$ , depend on  $Re$ ,  $ReSl$  and  $Re_p$ . This functional dependence may involve the determination of several coefficients, so let us consider the general least-square problem of finding the optimum  $n$ -parameters:  $h_1, h_2, \dots, h_n$ , that minimize the square error function:

$$E(h_1, h_2, \dots, h_n) := \sum_{\alpha=1}^m (f_T(t; h_1, h_2, \dots, h_n) - f_N^\alpha)^2, \quad (2.4.1)$$

where  $f_T$  is equation (2.2.6),  $f_N^\alpha$  is the numerical value at the corresponding time  $t$  and  $m$  is the number of data points used. To simplify the notation we will write  $h := \{h_1, h_2, \dots, h_n\}$  and also omit the dependence on the variables parameters, where there is no risk of confusion.

To find the minimum  $E$  we start with a point  $h^0$  and generate a sequence of points  $h^p$ ,  $p = 1, 2, \dots$ , which converges to the desired minimum. We use the Newton's method to determine a search direction  $\delta h^p$  and the next point in the Newton iteration is determined by:

$$h^{p+1} = h^p + \delta h^p, \quad (2.4.2)$$

where  $\delta h^p$  is given by

$$\delta h^p = -H(h^p)^{-1} g(h^p), \quad (2.4.3)$$

where  $g(h) = \mathcal{D}E(h)$  is the gradient of  $E$  and  $H(h) = \mathcal{D}^2E(h)$  is the Hessian matrix of  $E$ . In components, we have

$$g(h) = \left( \frac{\partial E}{\partial h_1}, \frac{\partial E}{\partial h_2}, \dots, \frac{\partial E}{\partial h_n} \right), \quad (2.4.4)$$

and

$$H(h) := \begin{bmatrix} \frac{\partial^2 E}{\partial h_1^2} & \dots & \frac{\partial^2 E}{\partial h_n \partial h_1} \\ \vdots & \ddots & \vdots \\ \frac{\partial^2 E}{\partial h_1 \partial h_n} & \dots & \frac{\partial^2 E}{\partial h_n^2} \end{bmatrix}. \quad (2.4.5)$$

The problem at hand is how to determine the gradient vector and the Hessian matrix. Let us start with the computation of the partial derivatives of  $E$ . For the first derivative we have

$$\frac{\partial E}{\partial h_i} = 2 \sum_{\alpha} (f_T(t_{\alpha}) - f_N^{\alpha}) \frac{\partial f_T}{\partial h_i}; \quad (2.4.6)$$

so, the gradient of  $E$  only requires the knowledge of  $\mathcal{D}f_T$ . As for the second derivative of  $E$  a simple computation yields:

$$\frac{\partial^2 E}{\partial h_j \partial h_i} = 2 \left[ \sum_{\alpha} \frac{\partial f_T}{\partial h_j} \frac{\partial f_T}{\partial h_i} + (f_T(t_{\alpha}) - f_N^{\alpha}) \frac{\partial^2 f_T}{\partial h_j \partial h_i} \right], \quad (2.4.7)$$

so that to compute the Hessian of  $E$  we need  $\mathcal{D}^2 f_T$  in addition to  $\mathcal{D}f_T$ . Thus, in order to compute  $g$ , and  $H$ , all that is needed is the computation of the gradient  $\mathcal{D}f_T$  and the Hessian  $\mathcal{D}^2 f_T$ .

The computation of these derivatives analytically would require some complicated calculations, namely the derivatives of the FO and VO differential operators with respect to the parameters  $h$ . To avoid this, we opt to follow a simple, general but still accurate procedure to obtain the derivatives using finite-differences.

$$\begin{aligned} \frac{\partial f_T}{\partial h_i} &\simeq \frac{1}{2\epsilon_i} [f_T(h_i + \epsilon_i) - f_T(h_i - \epsilon_i)] \\ \frac{\partial^2 f_T}{\partial h_i^2} &\simeq \frac{1}{2\epsilon_i^2} [f_T(h_i + \epsilon_i) - 2f_T(h_i) + f_T(h_i - \epsilon_i)] \\ \frac{\partial^2 f_T}{\partial h_i \partial h_j} &\simeq \frac{1}{4\epsilon_i \epsilon_j} \left[ f_T(h_i + \epsilon_i, h_j + \epsilon_j) - f_T(h_i - \epsilon_i, h_j + \epsilon_j) - \right. \\ &\quad \left. - f_T(h_i + \epsilon_i, h_j - \epsilon_j) + f_T(h_i - \epsilon_i, h_j - \epsilon_j) \right] \end{aligned} \quad (2.4.8)$$

where the  $\epsilon$ 's are in the range of  $10^{-4}$  to  $10^{-8}$ .

All these expressions demand the computation of a FO or VO derivative. As we have seen the derivative can be evaluated by solving an improper integral, since

its integrand is not bounded: it goes to infinity as  $\tau \rightarrow t$ . Nevertheless it can be computed numerically. A general method for this type of integrals can be found in [1]. We chose a second-order of accuracy quadrature that is valid for both the FO or VO operators. The only difference between them is that for the first,  $q$  is constant in time whereas for the second it varies. The approximation yields

$$\mathcal{D}^q \xi_n = \frac{\Delta\tau^{1-q}}{\Gamma(3-q)} \sum_{i=0}^n a_{i,n} \mathcal{D}^1 \xi_i + \frac{(\xi_{0+} - \xi_{0-}) \tau_n^q}{\Gamma(1-q)} \quad (2.4.9)$$

where

$$a_{i,n} = \begin{cases} (n-1)^{2-q} - (n+q-2)n^{1-q} & \text{if } i=0 \\ (n-i-1)^{2-q} - 2(n-i)^{2-q} + (n-i+1)^{2-q} & \text{if } 0 < i < n \\ 1 & \text{if } i=n \end{cases} \quad (2.4.10)$$

and  $\xi_i$  is the function computed at  $\tau = i \Delta\tau$  being  $\Delta\tau$  the time step. In the present work the second term in equation (2.4.9) drops out because  $\xi_{0+} = \xi_{0-} = 0$ .

At this point we have all the necessary tools, so it is appropriate to sum up the above procedure in an algorithm:

1. Input data points  $f_N^\alpha$ ;
2. Start with some guess  $h^0$
3. With  $h^0$  obtain  $f_T(t; h^0)$ ;
4. With  $h^0$  and  $f_T(t^\alpha; h^0)$  compute  $\frac{\partial f_T}{\partial h_i}$  and  $\frac{\partial^2 f_T}{\partial h_i \partial h_j}$ ;
5. Compute  $H(h^0)$  and  $g(h^0)$ ;
6. Solve  $H(h^0) \cdot \delta h^0 = -g(h^0)$ , where  $\delta h^0 := h^1 - h^0$ ;
7. Update the solution  $h^1 = h^0 + \delta h^0$  and repeat steps 3–6 with  $h^0 \leftarrow h^1$  until convergence.

# Chapter 3

## Numerical Methods

In this chapter, we describe the numerical approach used to solve the unsteady axisymmetric flow over the sphere. The numerical techniques include space and time discretization methods and a continuation method for non-linear equations. The present numerical method is an extension of Kobayashi and Pereira [12] to a novel implicit Newton-Krilov matrix-free multigrid solver for the unsteady, incompressible Navier-Stokes equations.

### 3.1 Introduction

We intend to simulate numerically the flow field generated by an oscillating flow around a fixed spherical particle. The flow is assumed to be incompressible and two-dimensional. The first assumption is reasonable since we are dealing with low speed flows when compared with the speed of sound. The last one is valid for laminar flows around axisymmetric geometries with an axisymmetric wake which is reasonable for  $Re$  less than 25.

There are many numerical methods suited to handle two-dimensional incompressible flows. These flows are often simulated using either the primitive variables formulation where the two components of the velocity and the pressure field are computed, or using the vorticity and stream function variables formulation.

In this work instead, we use the novel stream function method proposed by Kobayashi and Pereira [12].

### 3.1.1 Governing equations

Taking the rotational of the momentum equations gives rise to the equation for the vorticity vector field, which in two dimensional flows has an unique non-null component. Also for incompressible flows the velocity is the rotational of a potential vector - the stream function. In this formulation the vorticity is equal to the Laplacian of the stream function. So, by substituting the vorticity and the velocity dependence on the stream function in the equation for the vorticity gives rise to a equation whose sole variable is the stream function. Hence the original three equations, one continuity equation and two momentum equations, are reduced to a single equation. Moreover, the resulting equation possesses simpler and more physical boundary conditions than the traditional vorticity/stream function formulation.

The stream-function equation cast in a cylindrical coordinate system  $(r, z)$  for an axisymmetric formulation, is

$$\frac{\partial}{\partial t} (D^2\Psi) - \frac{\partial\Psi}{\partial z} \frac{\partial}{\partial r} (D^2\Psi) + \left( \frac{\partial\Psi}{\partial r} + \frac{\Psi}{r} \right) \frac{\partial}{\partial z} (D^2\Psi) + \frac{1}{r} \frac{\partial\Psi}{\partial z} D^2\Psi = \nu_f [D^2 (D^2\Psi)] \quad (3.1.1)$$

where the operator  $D^2$  is defined as:

$$D^2 = \nabla^2 - \frac{1}{r^2} \quad (3.1.2)$$

and  $\nabla^2$  is the usual Laplacian written in cylindrical coordinates,

$$\nabla^2 = \frac{1}{r} \frac{\partial}{\partial r} + \frac{\partial^2}{\partial r^2} + \frac{\partial^2}{\partial z^2} \quad (3.1.3)$$

The flow velocities  $U_r$  and  $U_z$  are related to  $\Psi$  by:

$$U_r = -\frac{\partial \Psi}{\partial z}, \quad U_z = \frac{\partial \Psi}{\partial r} + \frac{\Psi}{r} \quad (3.1.4)$$

The governing equation (3.1.1) is made dimensionless using the characteristic dimensions stated in (2.2.2) which yields

$$Sl \frac{\partial}{\partial t} (D^2 \psi) - \frac{\partial \psi}{\partial z} \frac{\partial}{\partial r} (D^2 \psi) + \left( \frac{\partial \psi}{\partial r} + \frac{\psi}{r} \right) \frac{\partial}{\partial z} (D^2 \psi) + \frac{1}{r} \frac{\partial \psi}{\partial z} D^2 \psi = \frac{1}{Re} [D^2 (D^2 \psi)] \quad (3.1.5)$$

### 3.1.2 Boundary conditions

Since we are dealing with a fourth-order differential equation (3.1.5) in space, we need two boundary conditions at each boundary.

At the outer boundary (line AB in figure 3.1) we have prescribed velocity  $\mathbf{U} = U \mathbf{e}_z = U_0 \sin(\omega t) \mathbf{e}_z$ , which in nondimensional form yields  $\mathbf{u} = \sin(9t) \mathbf{e}_z$ . Thus, using equations (3.1.4) in the nondimensional form, we obtain

$$-\frac{\partial \psi}{\partial z} = 0, \quad \frac{\partial \psi}{\partial r} + \frac{\psi}{r} = \sin(9t) \quad (3.1.6)$$

At the sphere surface (CD) there is no normal flow since it is a solid wall. Mathematically this condition is equivalent to a constant value for the stream function along this wall.

$$\psi = \text{constant} = 0 \quad (3.1.7)$$

The constant was set equal to zero since, like in a potential field, the stream function has an arbitrary zero-level.

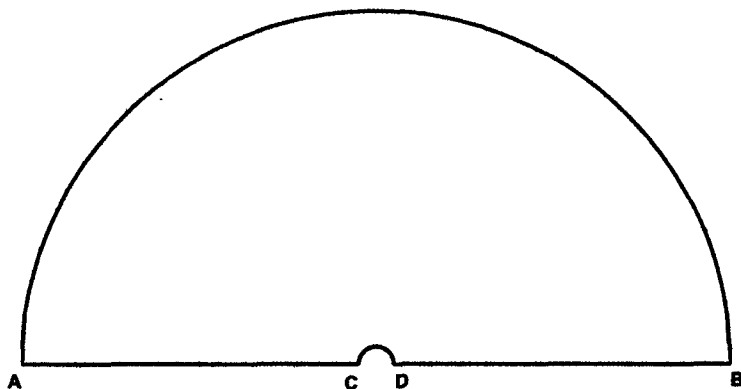


Figure 3.1: Geometry of the numerical domain

The second condition at this boundary is to nullify the normal gradient of the stream function which means that there is no tangential velocity at the sphere surface. This is the usual no-slip condition used for solid walls.

$$\frac{\partial \psi}{\partial n} = 0 \quad (3.1.8)$$

The remaining boundaries (AC and DB) are axisymmetry lines. At an axisymmetry line the vorticity ( $\zeta$ ) is null. From the relation between vorticity and stream function the we obtain the boundary equation

$$\zeta = \nabla^2 \psi = 0 \quad (3.1.9)$$

In addition, given that there is no fluid flow across this boundary,  $\psi$  is prescribed as a constant value along the boundary in the same manner as in a solid wall. Therefore the remaining boundary condition is given by equation (3.1.7).

## 3.2 Spatial discretization

The governing equation (3.1.5) can not be solved analytically. Thus some kind of discretization must be considered which will transform the original problem into a set of nonlinear algebraic equations suited to be solved iteratively.

In this section we present the spatial discretization. Here we use finite-differences to discretize the spatial derivatives. Two different schemes are used: the second-order finite-differences; and the fourth-order compact finite-differences.

The fourth-order scheme has a spectral-like resolution (see Lele [13]). In spectral methods like the Fourier transform, the value of the approximate derivatives is dependent on the derivatives at all nodes whereas in traditional finite-difference schemes, it depends solely on the values of neighbor nodes. The compact or Padé finite-difference schemes mimic the global dependence of spectral methods since the derivative approximation depends not only on the closest neighbor nodes values but also on the neighbors derivative values.

The second-order central finite-difference scheme is used for the preconditioning of the solver, which is a process that does not need high accuracy as we will explain in section 3.4. So, in that phase of the solver we take advantage of a less expensive discretization to save computational time.

### 3.2.1 Internal nodes

The first derivative is approximated by the following discrete form

$$\phi'_i + a_1 (\phi'_{i-1} + \phi'_{i+1}) = \frac{b_1}{h} (\phi_{i+1} - \phi_{i-1}) + o(h^p) \quad (3.2.1)$$

Here  $\phi$  is the dependent variable and  $\phi_i$  is the value at the node  $i$ . The independent variable at a node  $i$  is  $x_i = h(i - 1)$  where  $h$  is the uniform grid spacing.

It should be noted that the coefficient  $a_1$  couples the derivative at node  $i$  with its neighbors. In the traditional finite-difference approximation this coefficient is zero. For the compact schemes  $a_1$  is not zero leading to a set of linear equations that must be solved in order to obtain the  $\phi_i'$ 's. This is the reason why compact schemes have spectral-like resolution.

The coefficients in equation (3.2.1) are determined by requiring that the error be of an order of accuracy  $p$ . There are several ways to determine these values. We use a Taylor series expansion of the desired order and the method of undetermined coefficients. This method yields for the second-order scheme

$$a_1 = 0, \quad b_1 = 1/2$$

and

$$a_1 = 1/4, \quad b_1 = 3/4$$

for the fourth-order scheme.

A similar procedure for the second derivative leads to

$$\phi_i'' + a_2 (\phi_{i-1}'' + \phi_{i+1}'') = \frac{b_2}{h^2} (\phi_{i+1} - 2\phi_i + \phi_{i-1}) + o(h^p) \quad (3.2.2)$$

where

$$a_2 = 0, \quad b_2 = 1$$

for the second-order scheme and

$$a_2 = 1/10, \quad b_2 = 6/5$$

for the fourth-order scheme.

A remark should be made at this point: the governing equation (3.1.5) involves fourth-order derivatives and also several third-order cross derivatives, however we only discretize first and second spatial derivatives. These higher derivatives are computed by applying the first and the second derivative approximations.

### 3.2.2 Boundary nodes

The previous stencils are valid for an unbounded domain. At a boundary node the approximation must be modified such that it does not depend on nodes outside of the domain. Hence the left boundary scheme for the first derivative is:

$$\phi'_0 + \bar{a}_1 \phi'_1 = \frac{1}{h} (\bar{b}_1 \phi_0 + \bar{c}_1 \phi_1 + \bar{d}_1 \phi_2) + o(h^p) \quad (3.2.3)$$

and for the second derivative we have

$$\phi''_0 + \bar{a}_2 \phi''_1 = \frac{1}{h^2} (\bar{b}_2 \phi_0 + \bar{c}_2 \phi_1 + \bar{d}_2 \phi_2) + \frac{\bar{e}_2}{h} \phi'_0 + o(h^p) \quad (3.2.4)$$

The right boundary is handled in a similar manner.

Due to stability arguments, the order of accuracy is lowered one degree for the boundary schemes ([4]) yielding the coefficients

$$\bar{a}_1 = 2, \quad \bar{b}_1 = -15/16, \quad \bar{c}_1 = 2, \quad \bar{d}_1 = 1/2$$

for a third-order approximation, whereas in the case of the first-order approximation we do not need to approximate the value of the first derivative at the boundary.

For the second derivative the coefficients are:

$$\bar{a}_2 = 0, \quad \bar{b}_2 = -2, \quad \bar{c}_2 = 2, \quad \bar{d}_2 = 0, \quad \bar{e}_2 = -2$$

for second-order of accuracy and

$$\bar{a}_2 = 2, \quad \bar{b}_2 = -3/2, \quad \bar{c}_2 = 0, \quad \bar{d}_2 = 3/2, \quad \bar{e}_2 = -3$$

for fourth-order accuracy. Here it should be noted that the second derivative at the boundary depends on the value of the variable as well as its first derivative at the boundary. This is not a problem since the latter is prescribed at the boundary by the velocity. At the axisymmetry line (AC and DB), the second derivative itself is known and therefore no approximation is necessary.

### 3.3 Time discretization

Runge-Kutta methods seem a natural choice for the time marching scheme since they are very robust and require small storage capacity. We intend, however, to simulate flows with very small  $ReSl$ . This means that our diffusive coefficient  $1/ReSl$  may be quite large requiring the use of very small time steps to remain within the stability region of the Runge-Kutta methods (see Kobayashi [11] and Pereira and Pereira [21]).

To allow affordable time steps we developed several high-order implicit methods using the same underlying concept of the compact finite-difference methods for the spatial derivatives, *i.e.*, the derivative depends both on the variable and the derivative at the previous time steps. These methods demand more storage capacity than the Runge-Kutta methods, but the gain in stability and the fact that we use a matrix-free method largely compensate for the increase in memory requirements.

So, let us consider the general differential equation:

$$\frac{d\phi}{dt} = f(\phi, t) \tag{3.3.1}$$

Scheme	Order	$p$	$q$	$a_1$	$a_2$	$a_3$	$b_1$	$b_2$	$b_3$	$b_4$
1	4	3	2	19/9	-5/9	1/9	8/3	-8/3	-	-
2	4	3	3	7/6	-4/3	1/6	5/2	-4	3/2	-
3	3	3	1	8/5	-1/5	12/5	-12/5	-	-	-
4	3	1	4	-3/4	-	-	19/12	-27/8	9/4	-11/24
5	3	3	2	77/120	7/15	-5/24	19/10	-19/10	-	-

Table 3.1: Time discretization coefficients  $a_j$  and  $b_j$ .

We seek a time marching method given by the expression

$$\phi^{n+1} = \sum_{j=1}^p a_j \phi^{n+1-j} + \Delta t \sum_{j=1}^q b_j f^{n+2-j} \quad (3.3.2)$$

where

$$f^n = f(\phi^n, \Delta t(n-1)) \quad (3.3.3)$$

and  $\Delta t$  is the uniform time step, and  $n$  in the current time step.

Using this general form we develop expressions with third and fourth-order accuracy in time. The procedure is analogous to that used for the spatial derivative approximations: the Taylor series of the desired order is compared with (3.3.2) and the  $a_j$  and  $b_j$  are determined by equating coefficients.

Table 3.1 lists the coefficients and the order of accuracy of each scheme studied in this work. For schemes 2, 4 and 5 we let one of the coefficients  $a_j$ ,  $b_j$  be free and then adjust the other coefficients to maximize the stability region (see figures 3.2 and 3.3). The maximum order of accuracy we may obtain with a certain  $p$  and  $q$  is  $p+q-1$ , so for these three schemes, we sacrifice accuracy to obtain better stability properties.

These discrete forms were then used together with both spatial approximations, described previously in section 3.2 to discretize the one-dimensional convection-diffusion equation. Following standard methodology we determined the stability limits for each

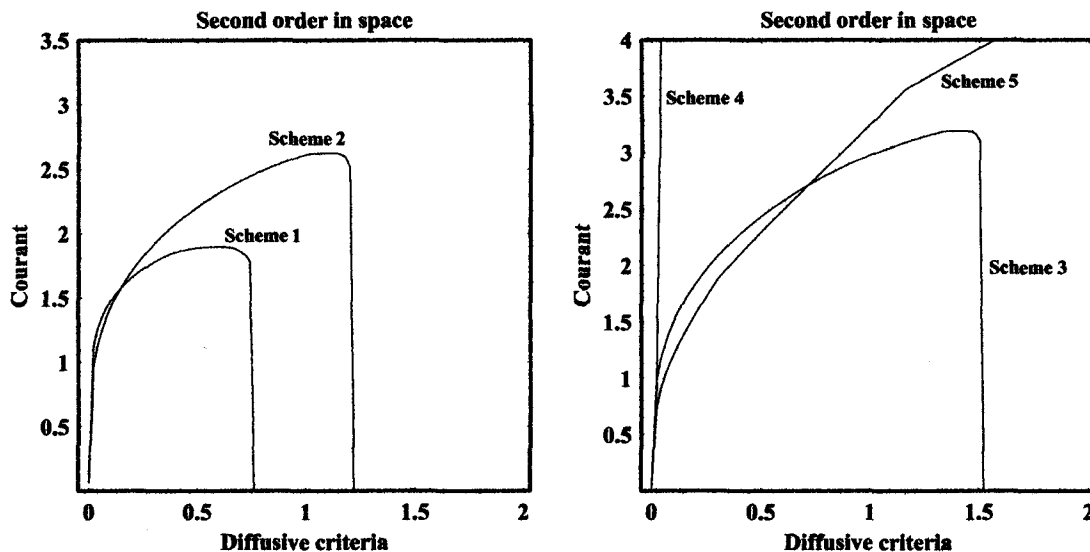


Figure 3.2: Stability region (to the right and below the lines) for each temporal discretization schemes. Second-order spatial approximation with: fourth-order in time (left), third-order in time (right).

discretization schemes as a function of the convective coefficient  $CFL = U_0 \Delta t / \Delta x$ , the so called *Courant-Friedrichs-Lewy* number and the diffusive parameter  $\tau_d = \Delta t / (ReSl\Delta x^2)$

These maps (figures 3.2 and 3.3) show that the fourth-order approximation for the time derivative displays a very small stability region independent of the spatial discretization used. In fact, these schemes are worse than the traditional Runge-Kutta methods, and therefore are ruled out from further consideration. On the other hand the third-order schemes 4 and 5 display very large stability regions. For these two approximations there is no limit of stability beyond a certain diffusivity number. In fact scheme 4 is virtually unconditionally stable. For this reason scheme 4 was selected for the numerical simulations.

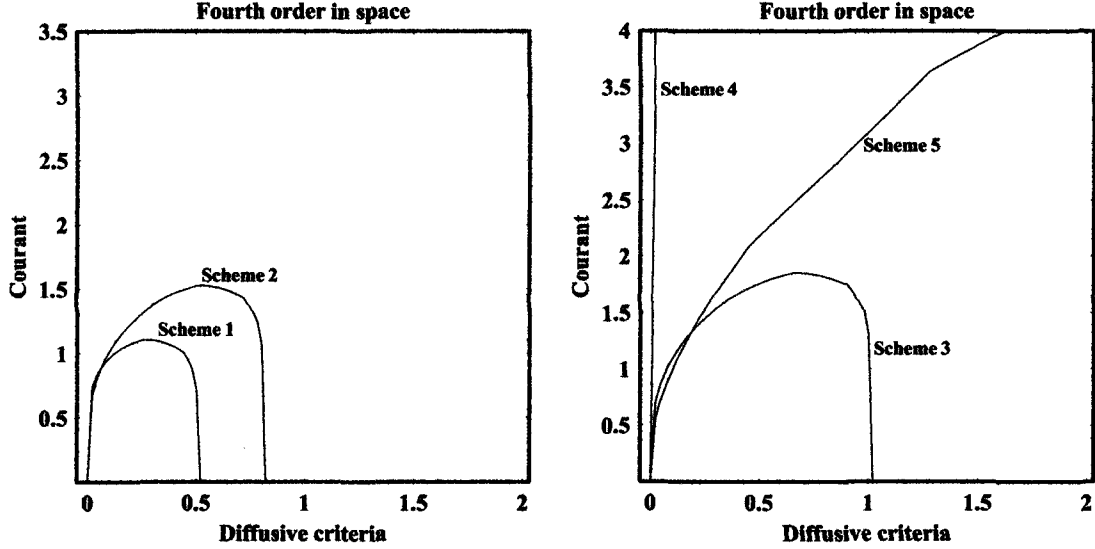


Figure 3.3: Stability region (to the right and below the lines) for each temporal discretization schemes. Fourth-order compact spatial approximation with: fourth-order in time (left), third-order in time (right).

### 3.4 The Solver: Newton-Krylov-multigrid matrix free method

The discrete form of the governing equations results in a system of nonlinear equations which are solved using Newton's method. We define the vectorial function  $\mathbf{N} : \mathbb{R}^N \rightarrow \mathbb{R}^N$  where  $N$  is the number of grid points, as

$$\begin{aligned} \mathbf{N}(\xi) = & Sl \frac{\partial}{\partial \tau t} (D_h^2 \xi) - \frac{\partial \xi}{\partial_{hz}} \frac{\partial}{\partial_{hr}} (D_h^2 \xi) + \left( \frac{\partial \xi}{\partial_{hr}} + \frac{\xi}{r} \right) \frac{\partial}{\partial_{hz}} (D_h^2 \xi) + \\ & + \frac{1}{r} \frac{\partial \xi}{\partial_{hz}} D_h^2 \xi - \frac{1}{Re} [D_h^2 (D_h^2 \xi)] \end{aligned} \quad (3.4.1)$$

for all  $\xi \in \mathbb{R}^N$ , where the subscripts  $h$  and  $\tau$  identify the discrete space and time forms of the differential operators in the governing equation. We seek to solve the equation  $\mathbf{N}(\xi) = 0$  using Newton's method which iterates according to the following

algorithm:

1. Start with an initial guess  $\psi_0$ , and set  $\xi_0 \leftarrow \psi_0$
2. Solve  $\text{DN}(\xi_0) \cdot \delta\xi = -\mathbf{N}(\xi_0)$
3. If  $\|\delta\xi\| < \epsilon_N$ ,  
then set  $\psi^{n+1} \leftarrow \xi_0 + \delta\xi$  and  $\text{Return}(\psi^{n+1})$   
else set  $\xi_0 \leftarrow \xi_0 + \delta\xi$  and proceed to step 2.

where  $\text{DN}$  is the Jacobian matrix,  $n$  is the Newton iteration number and  $\epsilon_N$  is a given prescribed precision, usually in the range of  $10^{-5}$  to  $10^{-8}$ .

In step 2, a linear system of equations must be solved. The choice of the compact discretization scheme produce a dense Jacobian matrix ( $\text{DN}$ ) whereas a second-order central method returns a penta-diagonal matrix. The inversion of a dense matrix can be troublesome when direct methods such as Gauss elimination are used and in addition, they require the storage of a  $N \times N$  square matrix which is also a disadvantage. For these reasons a Krylov iterative method is used to solve the linear system of equations to a given tolerance  $\epsilon_K$ . The Flexible inner-outer preconditioned Generalized Minimal RESidual method (FGMRES [23]) is the chosen solver.

FGMRES does not require the matrix  $\text{DN}(\xi_0)$  explicitly but instead requires the matrix vector multiplication  $\text{DN}(\xi_0) \cdot \eta$  which can be accurately approximate by

$$\text{DN}(\xi_0) \cdot \eta = \|\eta\| (\text{DN}(\xi_0) \cdot \hat{\eta}) \approx \|\eta\| \left( \frac{\mathbf{N}(\xi_0 + t\hat{\eta}) - \mathbf{N}(\xi_0)}{t} \right) \quad (3.4.2)$$

where  $\hat{\eta} = \eta/\|\eta\|$  and  $t > 0$  is a small parameter.

To increase the efficiency of the solver, a preconditioning procedure is used together with a multigrid strategy to accelerate convergence. The multigrid strategy

can be used as a solver or as a preconditioner. In a multigrid method, different approximations for the derivatives may be used at different grid levels.

In this work we use fourth-order compact schemes in the finest grid and the usual second-order finite-differences at all the other grid levels. This procedure does not affect the accuracy of the method, since the fourth-order scheme is retained in the finest grid. However, it strongly influences the convergence rate and reduces the CPU time by avoiding the inversion of tridiagonal matrices necessary in the compact scheme. More details about Newton-Krylov-Matrix-Free methods may be found in [23], [10] and [12].

# Chapter 4

## Results and discussion

In chapters 2 and 3, we introduced several numerical procedures that must be validated. In sections 4.1 and 4.2, we show several results that demonstrate the validity and accuracy of the numerical algorithms. In the remainder of this chapter we present the results of the new drag force model obtained with the FO and VO operators.

### 4.1 Validation of the numerical code

In this section we study the accuracy of the numerical code to solve the flow around the particle. In the first test case we solve numerically a problem which has a known analytical solution to verify the order of accuracy of the stream function and the velocity field. We also validate the results for the flow around the sphere by comparing the numerical results for the drag force with experimental data and analytical solutions.

#### 4.1.1 Order of accuracy

Our test problem is the Taylor vortex. The problem consists of a planar geometry, which means that the governing equation is not the one presented before (3.1.5) but

Grid	$\Psi$		$u$		$v$	
	Error	Order	Error	Order	Error	Order
$5 \times 5$	$8.40 \times 10^{-4}$	—	$1.48 \times 10^{-3}$	—	$1.48 \times 10^{-3}$	—
$11 \times 11$	$1.84 \times 10^{-5}$	5.51	$3.50 \times 10^{-5}$	5.41	$3.58 \times 10^{-5}$	5.37
$21 \times 21$	$5.42 \times 10^{-7}$	5.09	$1.20 \times 10^{-6}$	4.87	$1.22 \times 10^{-6}$	4.88
$41 \times 41$	$1.51 \times 10^{-8}$	5.17	$5.57 \times 10^{-8}$	4.43	$5.62 \times 10^{-8}$	4.44

Table 4.1: Error evolution ( $L_2$  norm) with the grid - fourth-order accuracy.

a simplified version in Cartesian coordinates.

$$\frac{\partial}{\partial t} (\nabla^2 \psi) + \frac{\partial \psi}{\partial y} \frac{\partial}{\partial x} (\nabla^2 \psi) - \frac{\partial \psi}{\partial x} \frac{\partial}{\partial y} (\nabla^2 \psi) = \frac{1}{Re} \nabla^2 (\nabla^2 \psi) \quad (4.1.1)$$

where

$$\nabla^2 = \frac{\partial^2}{\partial x^2} + \frac{\partial^2}{\partial y^2} \quad (4.1.2)$$

The problem is solved in the square domain  $[0, \pi] \times [0, \pi]$ . As boundary conditions, we use prescribed inflow and outflow at all boundaries, given by equations (4.1.3) and (4.1.4). The simulation was performed until the final time  $T = \pi Re/10$  was reached, with  $Re = 100$ . For this test case the characteristic time is  $t_c = a/U_0$  which means that  $Sl = 1$ .

The exact solution of the Taylor vortex is

$$\psi(x, y, t; Re) = \exp\left(\frac{-2t}{Re}\right) \cos(x) \cos(y) \quad (4.1.3)$$

with the velocities given by

$$\begin{aligned} u(x, y, t; Re) &= \frac{\partial \psi}{\partial y} = -\exp\left(\frac{-2t}{Re}\right) \cos(x) \sin(y) \\ v(x, y, t; Re) &= -\frac{\partial \psi}{\partial x} = \exp\left(\frac{-2t}{Re}\right) \sin(x) \cos(y) \end{aligned} \quad (4.1.4)$$

We computed the numerical solution for four uniform square grids consisting of 5, 11, 21, 41 side nodes. Time step was set by imposing CFL=5 for all grids.

Grid	$\Psi$		$u$		$v$	
	Error	Order	Error	Order	Error	Order
$5 \times 5$	$3.54 \times 10^{-4}$	—	$2.54 \times 10^{-2}$	—	$2.54 \times 10^{-2}$	—
$11 \times 11$	$2.31 \times 10^{-5}$	3.94	$5.30 \times 10^{-3}$	2.26	$5.30 \times 10^{-3}$	2.26
$21 \times 21$	$3.26 \times 10^{-6}$	2.81	$1.21 \times 10^{-3}$	2.13	$1.21 \times 10^{-3}$	2.13
$41 \times 41$	$6.36 \times 10^{-7}$	2.37	$2.87 \times 10^{-4}$	2.08	$2.87 \times 10^{-4}$	2.08

Table 4.2: Error evolution ( $L_2$  norm) with the grid - second-order accuracy.

Tables 4.1 and 4.2 list the error norms of the numerical solution for the stream function and velocities. There is a very good agreement between the numerical and analytical solutions. The error decays as expected, namely with the fourth power of the grid parameter for the compact fourth-order scheme, and with the second power for the second-order finite-difference scheme.

#### 4.1.2 Sphere drag validation

The analysis presented above verifies the accuracy of the numerical code, hence we are certain that the stream function and the velocities are computed accurately. But in this work we intend to obtain the sphere drag as final output. By integrating the normal and shear stress over the spherical surface, the nondimensional force  $f_N$  acting on the particle computed from the numerical flow field is

$$f_N = \frac{D}{6\pi\mu_f a U_0} = \frac{1}{3} \int_0^\pi [-\bar{p}(1, \theta) - \bar{\tau}_{r\theta}(1, \theta) \sin \theta] \sin \theta d\theta \quad (4.1.5)$$

where the nondimensional pressure and friction components are given, in terms of the nondimensional stream function, by

$$\bar{p}(1, \theta) = \int_0^\theta \frac{\partial^3(\psi r)}{\partial r^3} \Big|_{r=1} d\theta \quad (4.1.6)$$

$$\bar{\tau}_{r\theta}(1, \theta) = \frac{\partial^2(\psi r)}{\partial r^2} \Big|_{r=1} \quad (4.1.7)$$

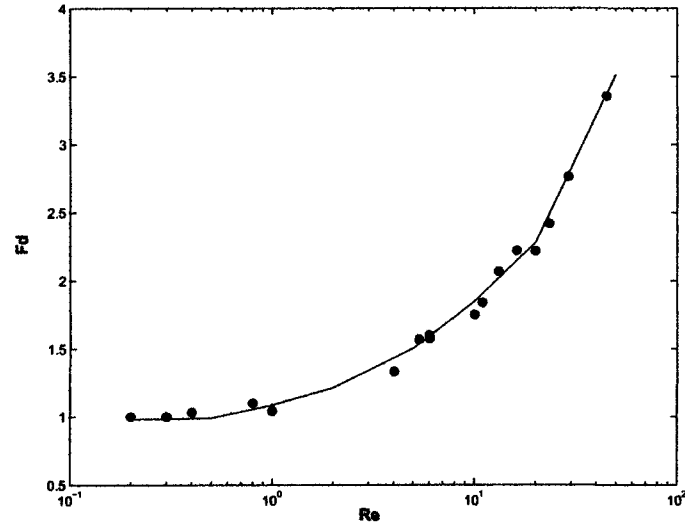


Figure 4.1: Drag experienced by the sphere for a steady flow as function of  $Re$ . Line: numerical solution. Dots: experimental data.

Note that the force is scaled by the steady Stokes drag  $6\pi\mu_f a U_0$ . This way the result is consistent with the nondimensional equations in section 1.2.

The integral is evaluated by the fourth-order Simpson's rule, the results are plotted in figure 4.1 against experimental data obtained by Castleman [24]. This comparison shows the high accuracy of the numerical method.

A grid independence study was carried out from which we conclude that a  $65 \times 129$  nodes, polar axisymmetric grid is necessary to attain the desired accuracy. Also the sensitivity to the outer boundary placement was studied showing that placing this boundary at 20 radii from the center of the sphere is enough to avoid undesirable boundary effects. In figure 4.2 the flow field is depicted for four different and gradually increasing Reynolds numbers. It clearly shows the growing of the wake which must not be affected by the presence of the boundary.

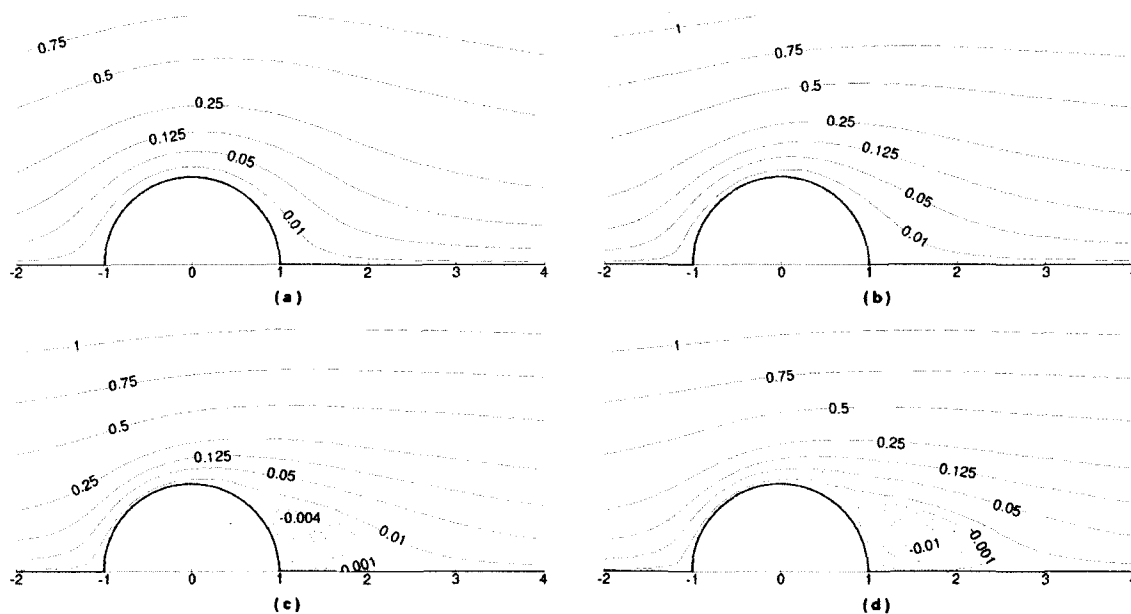


Figure 4.2: Stream lines for several Reynolds. (a)  $Re = 1.0$ , (b)  $Re = 10$ , (c)  $Re = 40$ , (d)  $Re = 50$

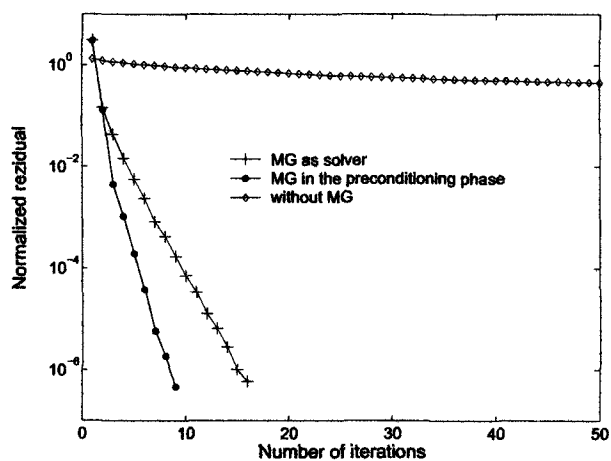


Figure 4.3: Multigrid effect on the convergence history

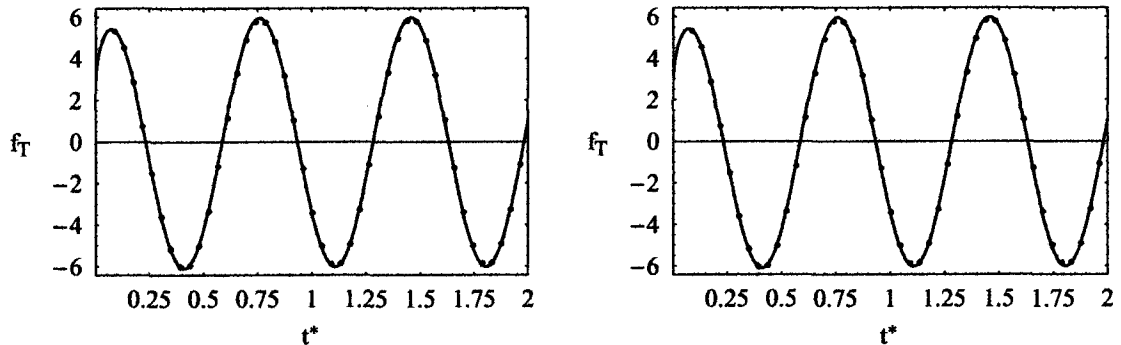


Figure 4.4: Drag experienced by the sphere for an unsteady flow with  $ReSl = 1$  and  $Re = 0.01$  (left) and  $Re = 0.1$  (right). Line: analytic solution. Dots: numerical data.

We also studied the influence of the multigrid on the convergence history. Figure 4.3 clearly shows that the multigrid is essential to the efficiency of the solver. The same figure also shows that when the multigrid is used in the preconditioning phase the convergence is faster than when it is used as a solver. We observe, however, that using the multigrid as preconditioner demands more CPU time per iteration.

To validate the unsteady drag force, a combination of a small Reynolds number  $Re = \{0.01, 0.1\}$  and a Reynolds-Strouhal number close to the unity  $ReSl = \{1, 2\}$  is chosen to ensure the validity of the analytical creeping flow equation (2.2.3). Again the numerical solution is in excellent agreement with the reference analytical results as figures 4.4 and 4.5 show. Note the quasi-independence of the force on  $Re$  for these low values of Reynolds numbers.

In summary, this test cases clearly show the accuracy and reliability of the model used in the numerical simulations.

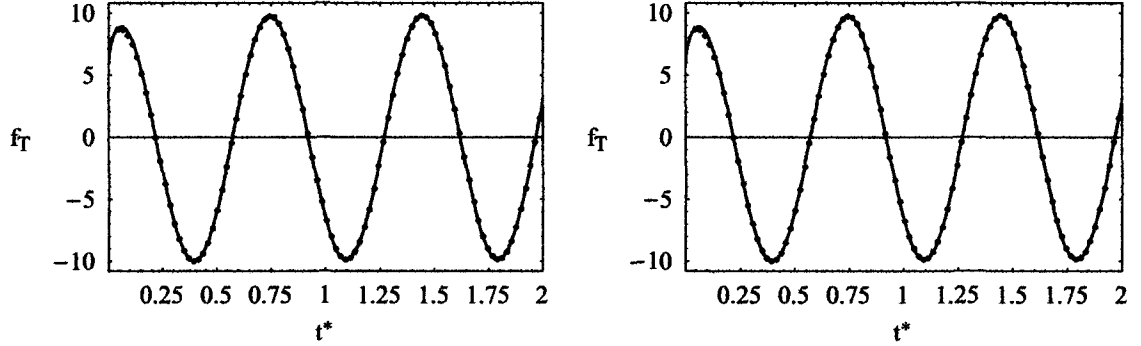


Figure 4.5: Drag experienced by the sphere for an unsteady flow with  $ReSl = 2$  and  $Re = 0.01$  (left) and  $Re = 0.1$  (right). Line: analytic solution. Dots: numerical data.

## 4.2 Validation of the least-squares method

To validate the least-squares algorithm presented in chapter 2, we determine  $F$  and  $q$  analytically from the creeping flow equation (2.2.5) for a sinusoidal flow

$$u(t) = \sin 9t = \text{Im}\{exp(i9t)\} \quad (4.2.1)$$

Substituting (4.2.1) this into (2.2.5) and (2.2.6) and equating both equations,  $F$  and  $q$  may be determined.

$$u + \sqrt{ReSl} \mathcal{D}^{\frac{1}{2}}u = F\mathcal{D}^q u \quad (4.2.2)$$

Applying the Laplace transform of the FO differential operator given in detail in [22], (4.2.2) becomes

$$exp(i9t) + \sqrt{ReSl} (i9)^{1/2} exp(i9t) = F(i9)^q exp(i9t) \quad (4.2.3)$$

which may be written as

$$1 + \sqrt{3ReSl} \left( \frac{\sqrt{2}}{2} + i\frac{\sqrt{2}}{2} \right) = F(9)^q \left( \cos \frac{\pi}{2}q + i \sin \frac{\pi}{2}q \right) \quad (4.2.4)$$

Equating imaginary and real parts of (4.2.4) yields

$$q = \frac{2}{\pi} \arctan \left( \frac{\sqrt{ReSl}}{\sqrt{2/3 + \sqrt{ReSl}}} \right) \quad (4.2.5)$$

$$F = \left(1 + \sqrt{18ReSl}\right) 9^{-\frac{2}{\pi} \arctan \left( \frac{\sqrt{ReSl}}{\sqrt{2/3 + \sqrt{ReSl}}} \right)} \sqrt{1 + \frac{9ReSl}{\left(\sqrt{2} + \sqrt{9ReSl}\right)^2}} \quad (4.2.6)$$

In figure 4.6 we compare the values of  $F$  and  $q$  obtained using the least-squares method against the analytical values (4.2.5, 4.2.6). The results computed with the least-square method and the analytical expressions are virtually indistinguishable from one another, clearly showing the accuracy and suitability of the least-squares method to determine  $q$  and  $F$ .

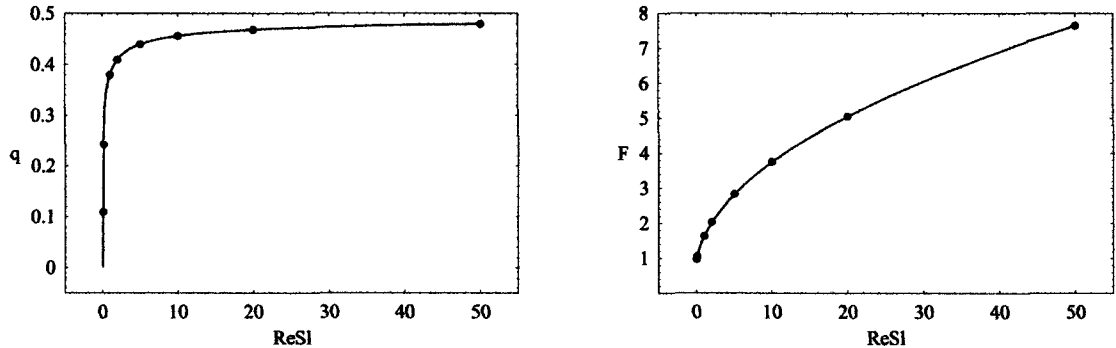


Figure 4.6: Verification of our optimization method. Left: FO-derivative order function of  $ReSl$ . Right: FO-derivative coefficient function of  $ReSl$ . Line: analytical result. Dots: numerical result.

### 4.3 Modeling of the hydrodynamic force

With the numerical codes properly verified we ran several flow configurations in order to determine the differential operator in our model as a function of  $Re$  and  $ReSl$ . The

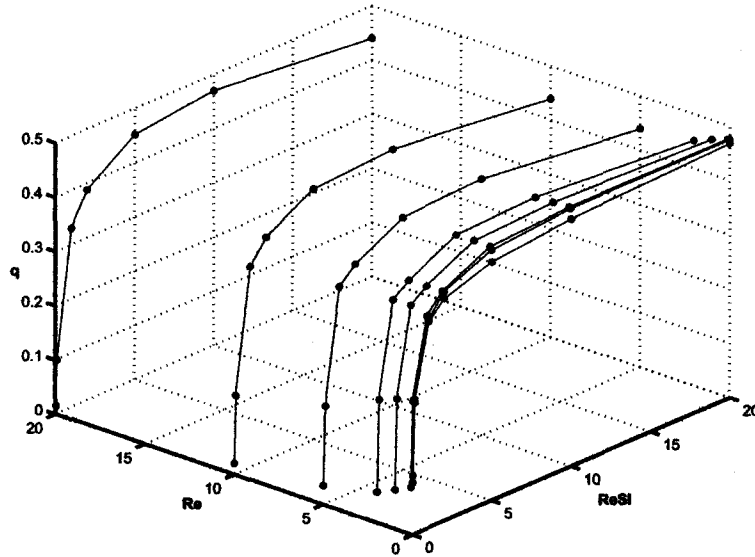


Figure 4.7: Drag  $q$ -order as a function of  $ReSl$  and  $Re$

runs covered oscillating flow in the range of  $0.01 \leq Re \leq 25$  and  $0.01 \leq ReSl \leq 25$ .

### 4.3.1 Fractional-Order

We hypothesize that the differential operator that models the viscous drag must be as simple as possible in order to be easily interpreted. So, we first assume  $q$  and  $F$  to be functions of  $Re$  and  $ReSl$  only, that is  $q = q(Re, ReSl)$  and  $F = F(Re, ReSl)$ . In other words, we look for a constant, non-integer order derivative (FO) relating the velocity of the flow and the sphere drag. As we have seen, in this work, the FO is a particular case of the VO operator.

The values of the derivative order  $q$  and coefficient  $F$  for different combinations of  $Re$  and  $ReSl$  were determined using the least-squares method previously described and verified in section 4.2. Figures 4.7 and 4.8 show the resulting maps for  $q$  and  $F$ . Figure 4.7 clearly shows that  $q$ , the order of the derivative, depends strongly on

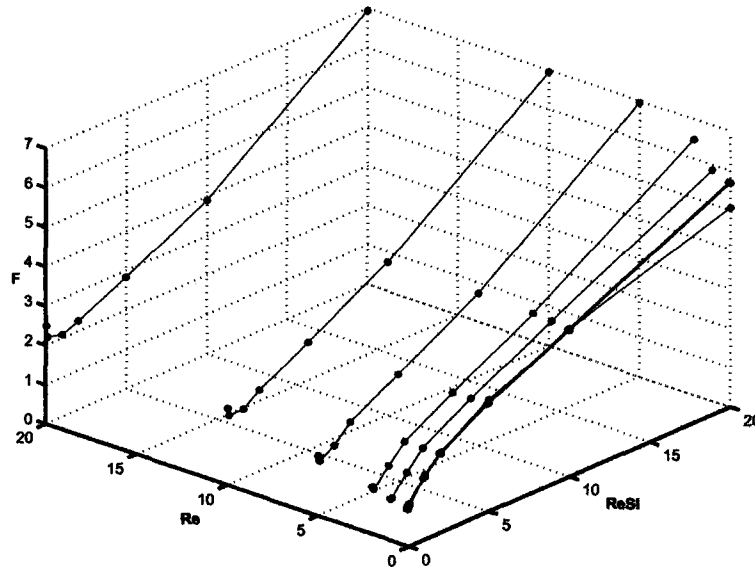


Figure 4.8: Drag  $F$ -coefficient as a function of  $ReSl$  and  $Re$

$ReSl$ . This variation with  $ReSl$  predicts that the drag force approaches the stationary drag as  $ReSl$  tends to 0 (stationary flow) and that the drag is dominated by history effects at higher values of  $ReSl$ . This behavior is readily explained if we recall that the history effects are brought about by the local acceleration term in the Navier-Stokes equation (or in the stream function equation) which in nondimensional form is multiplied by  $ReSl$ , as we may see in the governing equation (3.1.5).

On the other hand  $q$  depends only weakly on  $Re$ . Figure 4.7 shows that increasing  $Re$  leads to a slight increase in the memory effect ( $q$  decreases) at the high range of  $ReSl$ , but a moderate decrease in the memory effect ( $q$  increases) at the low  $Re$  regime.

Figure 4.8 shows that  $F$  depends strongly on both  $Re$  and  $ReSl$ . For high values of  $ReSl$ , the effect of  $Re$  tends to be minor, with a plateau at its highest end. At low

$Re$  the effect of  $Re$  is more pronounced and shows a tendency of  $F$  to increase with increasing  $Re$ .

The significance of these maps stems from the rendering of the complex interplay of the convection, local acceleration, viscous and pressure forces in a suggestive graphic form.

With the constant fractional-order model of the drag force we also can address an outstanding issue, namely, assessing the region of validity of the equations for the creeping flow with a sinusoidal background flow. As mentioned before these analytical solutions are restricted to infinitesimal  $Re$  and moderate  $ReSl$ , but the actual limiting boundaries in the  $Re \times ReSl$  plane have not been determined to date. Also, within the broader context of VO calculus we may also determine the boundary in the  $Re \times ReSl$  plane for the validity of the constant-order fractional-derivative model adopted in this sub-section. In order to determine these boundaries we have to define an error threshold for the acceptance of the model. Here the creeping flow or the constant-order model are accepted if the maximum difference between the predicted drag using the model and the result with the numerical simulation is less than one percent. Figure 4.9 shows the regions of validity of the creeping flow equation and the constant FO approximation of the drag.

This map shows that the unsteady creeping flow equation is also valid for finite  $Re$  numbers. This result is not surprising since the creeping flow equation for steady flow returns good results for  $0 < Re < 1$ . The map in figure 4.9 also shows that for higher  $Re$  and small  $ReSl$  the VO differential operator is necessary to accurately model the hydrodynamic force. As will be seen, this is a consequence of the increasing complexity of the flow field due to the fact that the convection dominates the flow

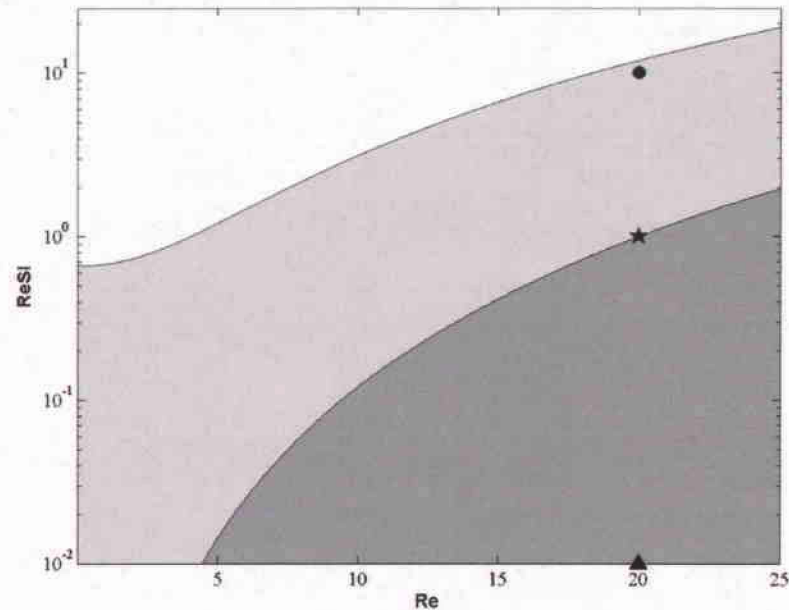


Figure 4.9: Region of validity of creeping flow equation (white), FO drag model (light grey + white), and VO drag model (dark grey)

in this region of the  $Re \times ReSl$  plane. In an intermediate region the FO differential kernel accurately models the force variation. This effect is displayed in figures 4.10, 4.11 and 4.12. In figure 4.10, the creeping flow equation returns good results even though  $Re = 20$  and  $ReSl = 10$ . When  $ReSl$  decreases to 1, the convective term becomes more important and the hydrodynamic force departs from the creeping flow equation, as depicted in figure 4.12. Decreasing further  $ReSl$  number to 0.01 the numerical solution shows a much more complex behavior which the FO operator is unable to represent. For this region a VO operator must be used to model accurately the hydrodynamic force.

For the low  $ReSl$  and moderate  $Re$  range, the flow around the sphere is much

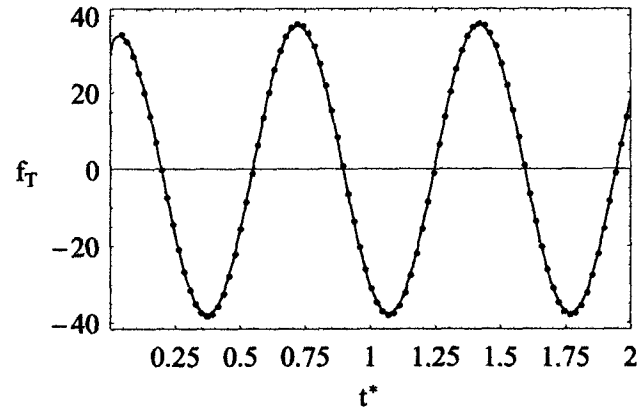


Figure 4.10: Sphere drag for  $Re = 20$ ,  $ReSl = 10$  ( $\bullet$  in the figure 4.9). Line: creeping flow equation (2.2.3), dots: numerical solution.

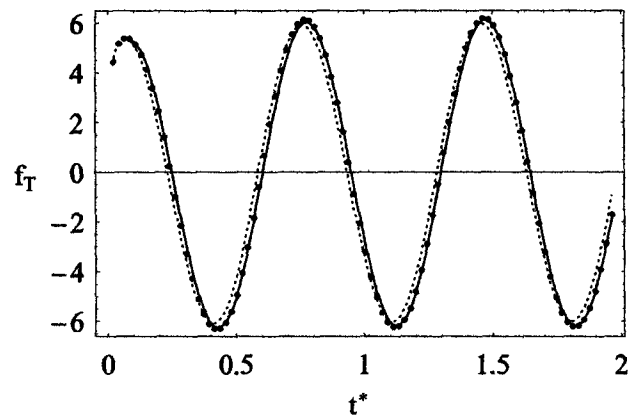


Figure 4.11: Sphere drag for  $Re = 20$ ,  $ReSl = 1$  ( $\star$  in the figure 4.9). Dash line: creeping flow equation (2.2.3), solid line: FO equation (2.2.6) with  $q = 0.365$ ,  $F = 1.94$ , dots: numerical solution.

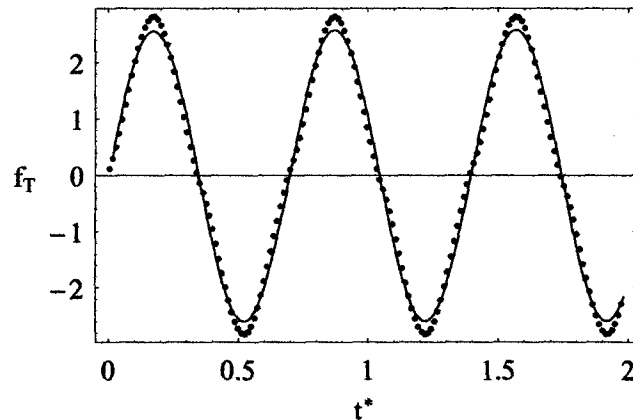


Figure 4.12: Sphere drag for  $Re = 20$ ,  $ReSl = 0.01$  ( $\blacktriangle$  in the figure 4.9). Solid line: FO equation (2.2.6) with  $q = 0.021$ ,  $F = 2.47$ , dots: numerical solution.

more complex as the flow detaches from the spherical surface and a recirculation zone is observed. In contrast, for low Reynolds numbers, the fluid can easily flow around the obstacle and no recirculation zone is observed. Figure 4.14 shows the snapshots of the flow at several instants of the oscillatory flow for  $Re = 20$ ,  $ReSl = 0.01$ . Here the flow is mainly influenced by convection and large recirculation zones are observed. Figure 4.13 shows the snapshots of the flow at several instants of the oscillatory flow for  $Re = 0.01$ ,  $ReSl = 0.01$ . For this case, diffusion and local acceleration dominate the flow which is fairly simple.

### 4.3.2 Variable-Order

As we have seen the increasing complexity of the flow is observed in the evolution of the drag on the sphere. The FO operator cannot capture this rich behavior. The natural step to overcome this limitation is to consider a VO differential operator instead of a FO operator to model the drag when convection dominates the flow.

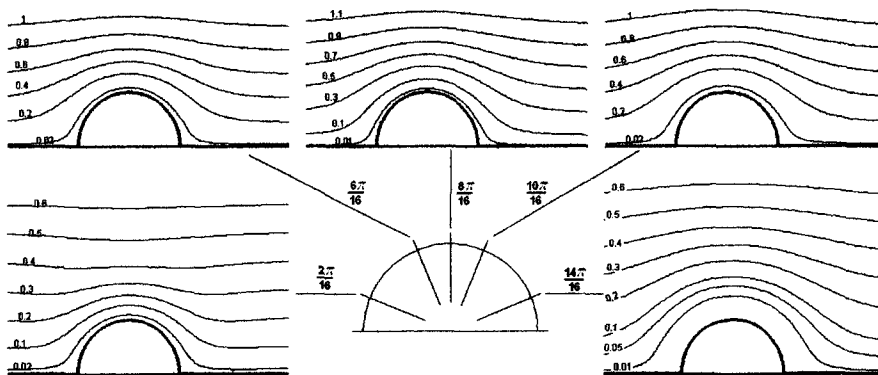


Figure 4.13: Snapshots of the flow at several instants  $t = \phi/9$  with  $\phi = \{2\pi/16, 6\pi/16, 8\pi/16, 10\pi/16, 14\pi/16\}$  for the oscillatory background flow  $u(t) = \sin(9t)$ , for  $Re = 0.01$ ,  $ReSl = 0.01$ .

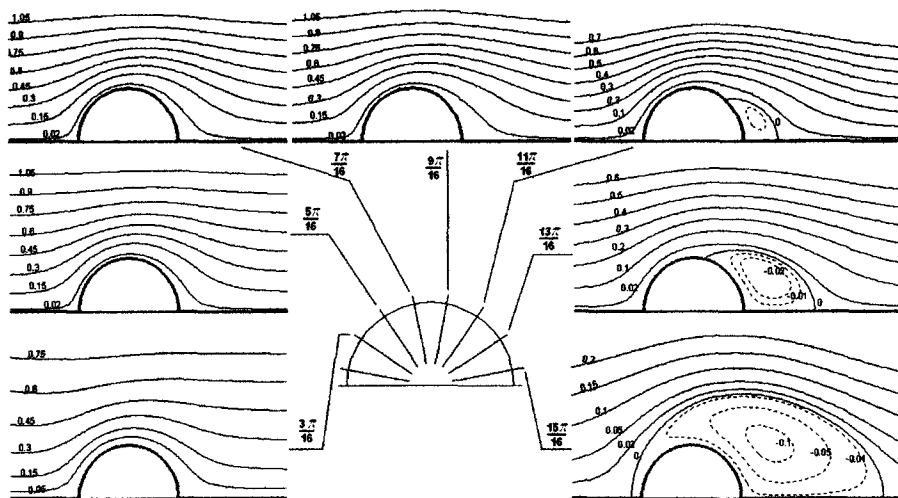


Figure 4.14: Snapshots of the flow at several instants  $t = \phi/9$  with  $\phi = \{3\pi/16, 5\pi/16, 7\pi/16, 9\pi/16, 11\pi/16, 13\pi/16, 15\pi/16\}$  for the oscillatory background flow  $u(t) = \sin(9t)$ , for  $Re = 20$ ,  $ReSl = 0.01$ .

The problem now is to find an appropriate definition for the variable-order of the differential operator. For the FO operator, we made  $q$  depend on a global  $Re$  and  $ReSl$ . But for higher  $Re$  the instantaneous flow velocity dictates the complexity of the flow and consequently the sphere drag. Therefore a natural candidate for the VO is to make  $q$  a function of the instantaneous Reynolds number  $Re_p = (aU_0/\nu_f) u(t) = Re u(t)$  or, equivalently, a function of instantaneous velocity. Thus we seek to determine

$$q(Re_p, Re, ReSl) = a_1(Re, ReSl) + a_2(Re, ReSl) |u|^{a_3(Re, ReSl)} \quad (4.3.1)$$

We choose this form for  $q$  based on the expected dependence on  $Re$ . We know that  $q$  approaches a constant value in the limit of small  $Re$ , thus a constant  $a_1$  is considered plus a function that goes to zero as  $Re$  becomes small,  $a_2 |u|^{a_3}$ . The latter functional form proves to give accurate results when compared with the numerical data. Another motivation for our choice of (4.3.1) for  $q$  is the fact that this functional form is commonly found in the expressions that extend the steady Stokes drag to finite  $Re$  numbers, see for example, Schiller and Naumann [24]

$$Cd_{steady} = \frac{24}{Re_d} (1 + 0.15 Re_d^{0.687})$$

The coefficient of the VO operator, once again designated as  $F$ , is maintained in the same form as in previous section. This choice is dictated by the fact that the key argument in this work is the physical interpretation of the derivative, so there is no strong reason for  $F$  to depend on  $Re_p$  thus we seek the simplest case. Therefore, we have again  $F = F(Re, ReSl)$ .

Once the expression for the VO differential operator is determined we compute the coefficients  $a_1$ ,  $a_2$ ,  $a_3$  and  $F$  using the least-squares method. For  $ReSl = 0.01$

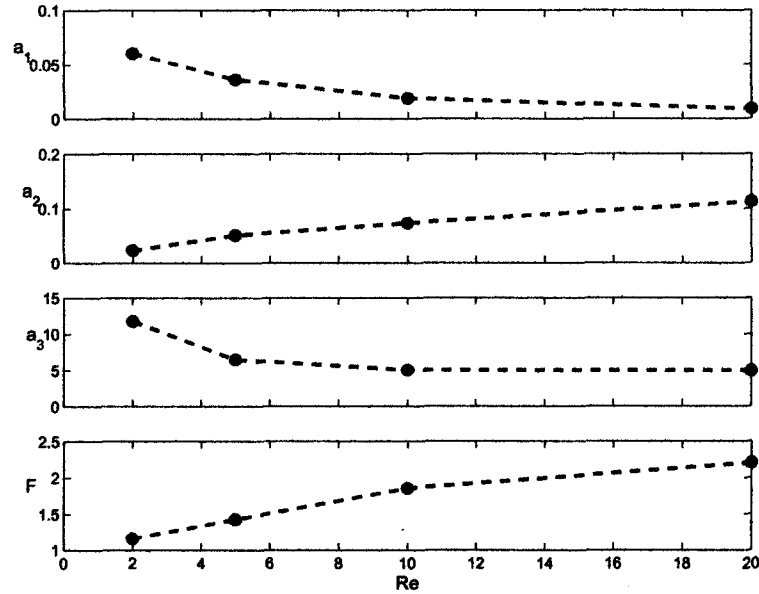


Figure 4.15: Coefficients  $a_1$ ,  $a_2$ ,  $a_3$  and  $F$  for  $ReSl=0.01$

the coefficients are shown in figure 4.15 as a function of  $Re$ . The values are plotted for  $Re \geq 2$  since below this limit the FO derivative is an accurate model of the drag force.

From figure 4.15 we observe that the coefficient  $a_2$  becomes more important with increasing  $Re$ . The dependence of the order of the derivative on the local flow velocity becomes stronger. The coefficient  $a_1$  decreases with increasing  $Re$  which means that the constant term of the VO operator is less important for higher  $Re$  and the memory effect grows in importance. The remaining coefficient  $a_3$  shows a strong dependence on  $Re$ , decreasing when it increases. The coefficient  $F$  varies with  $Re$  almost in the same manner as for the FO operator.

These values are then used to compute the hydrodynamic force acting on the

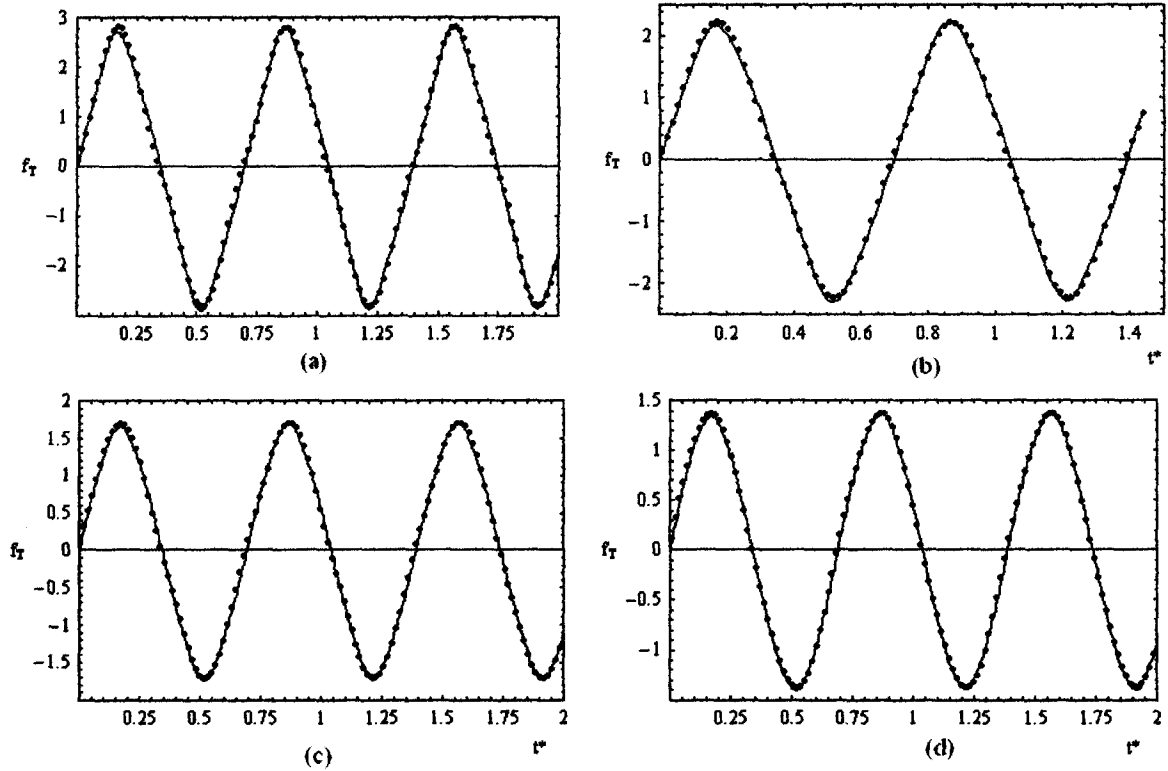


Figure 4.16: Sphere drag for  $ReSl = 0.01$  using the VO derivative in the drag model for several  $Re$ : (a)  $Re = 20$ , (b)  $Re = 10$ , (d)  $Re = 5$  and (c)  $Re = 2$ . The drag is computed with (2.2.6) and  $q$  is given by (4.3.1)

spherical particle. Figure 4.16 shows good agreement obtained when the VO differential operator is used for this convection dominated flow regime.

It should be noted that figure 4.16(a) is same case shown in figure 4.10, but now using the VO differential operator. As can be seen, the VO captures the behavior of the hydrodynamic force more accurately than the FO model.

Finally, in figure 4.17 we plot  $q$  as function of  $t$  and  $Re$  for the  $ReSl = 0.01$ . This map is very interesting since it synthesizes the complexity of the flow measured by

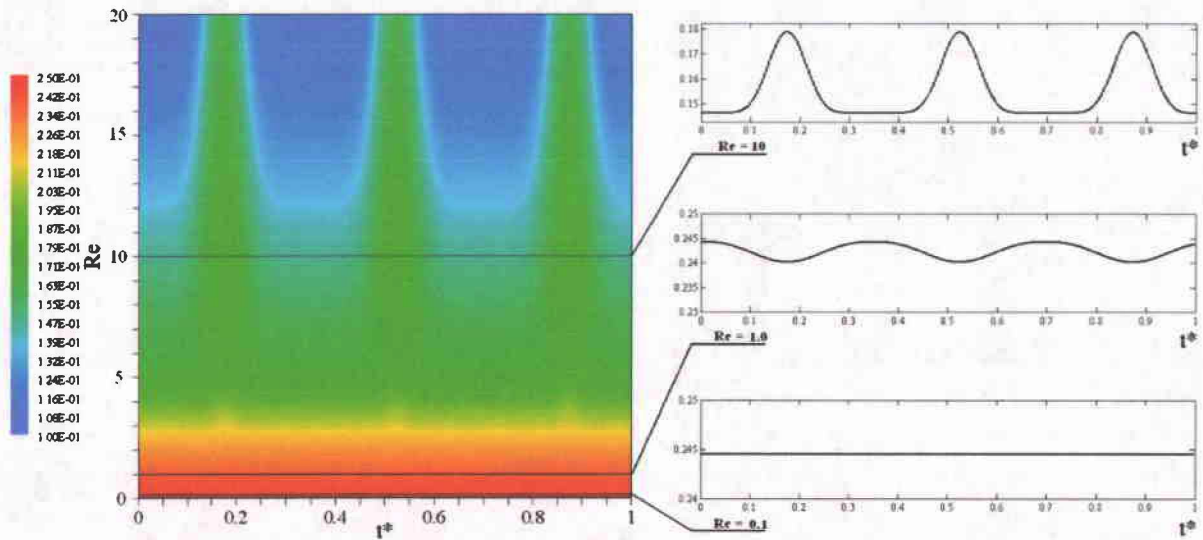


Figure 4.17: Order of the derivative  $q$  as a function of  $t$  and  $Re$  for  $ReSl = 0.01$ .  $q$  is given by (4.3.1) for  $Re > 1$ , otherwise  $q$  is the constant value determined with the FO model shown in figure 4.7.

the order  $q$  of the differential operator.

All the conclusions drawn before can be related to this map: for low  $Re$  the variable-order derivative tends to a constant-order derivative, and increasing  $Re$  makes the dependence of  $q$  on  $u(t)$  stronger. If we recall the snapshots of the flow field in figures 4.13 and 4.14 for this same value of  $ReSl$  we can conclude that the flow complexity is intimately related to the order of the derivative of the hydrodynamic force model.

# Chapter 5

## Conclusions and Future Work

The objective of this thesis is to use Fractional-Order and Variable-Order differential operators to model the hydrodynamic drag force acting on a fixed spherical particle under an oscillating flow at finite Reynolds and Strouhal numbers. From the work presented in this thesis we can draw the following conclusions:

(i) The creeping flow equation is valid for finite  $Re$  numbers. This was expected since the same phenomenon is observed for the steady creeping flow equation which returns good results for  $Re$  up to 1. It was also show that for higher  $Re$  and small  $ReSl$  the VO differential operator is the only operator that returns accurate results. It was concluded that the FO differential operator is valid in the intermediate parameter range between creeping flow and the VO model.

(ii) When the flow frequency goes to zero (steady flow) the differential operator (CO or VO) goes to zero independently of  $Re$  in the range investigated. This way the steady Stokes drag is recovered. When  $ReSl$  increases, the order of the differential operator tends to one-half. In conclusion, the main effect of the variation of  $ReSl$  is represented by the variation of the magnitude of  $q$  between 0 and 1/2. On other hand  $Re$  is responsible mainly for determining whether the differential operator is constant

or variable. For low  $Re$ , independent of  $ReSl$ , a CO differential operator models the hydrodynamic force accurately whereas for  $Re$  higher than 5 and small  $ReSl$ , only a VO differential operator returns accurate results.

(iii) The study of the flow field shows a close connection with the model differential operator. For higher  $Re$  and small  $ReSl$ , convection dominates the flow causing larger recirculating zones that increase the flow complexity and consequently increase the complexity of the force in-cycle variation. For this regime, a variable-order differential operator is necessary whereas for regimes of low convection the flow, a constant-order differential operator models the force accurately. This fact allows the conclusion that the complexity of the order of the derivative is connected with the flow field complexity. It must be stressed that this is one of the main advantages of this new approach: the order of the derivative is closely related to the physics of the flow field.

(iv) Also, we can conclude that the FO and VO differential operators are suited to treating nonlinear problems such the one here reported. Their simplicity and physical interpretation offer a large modeling potential.

(v) The implicit, high order numerical method developed to compute the flow around the particle is accurate and has very good stability properties.

The potential of fractional-order and variable order differential operators to capture complex, nonlinear behavior is particularly useful when studying complex problems in fluid dynamics. There are additional problems that may follow as a natural consequence of the work presented here.

The immediate generalization of the problem solved here is to consider a free particle. The problem is very similar to this one but the equation of motion for the particle must be solved together with the flow field. Then, the particle motion and

the flow around the particle are coupled since the flow around the particle depends on the relative velocity between sphere and fluid. The coupling of equations is an important numerical topic of research, making this problem even more challenging. For this case, the differential operator is expected to depend also on the relative density between the particle and the fluid.

Also related to this work is the hydrodynamic force acting on bubbles. The problem is very similar to the one here reported. However new phenomena must be taken into account, namely: deformable geometry, flow inside of the bubble and new boundary conditions at the bubble surface.

Another interesting problem is the free evaporating droplet. The characterization of the heat and mass transfer to and from the droplet would be very useful in determining the life-time of the droplet.

We anticipate that the methodology introduced in this work will be useful in addressing such problems.

# Bibliography

- [1] K. ATKINSON, *The numerical solution of Fredholm integral equations of the second kind*, SIAM J. Numer. Anal., 4 (1967), pp. 337–348.
- [2] A. B. BASSET, *A Treatise on Hydrodynamics*, vol. 2, Dover, 1888.
- [3] J. BOUSSINESQ, *Theorie Analytique de la Chaleur*, vol. 2, L'École Polytechnique, Paris, 1903.
- [4] M. H. CARPENTER, *The stability of numerical boundary treatments for compact high-order finite-differences schemes.*, Journal of Computational Physics, 108 (1993), pp. 272 – 295.
- [5] E. CHANG AND M. MAXEY, *Accelerated motion of rigid spheres in unsteady flow at low to moderate reynolds numbers. part 1. oscillatory motion.*, Journal of Fluid Mechanics, 277 (1994), pp. 347 – 379.
- [6] —, *Unsteady flow about a sphere at low to moderate reynolds numbers. part 2. accelerated motion.*, Journal of Fluid Mechanics, 303 (1995), pp. 133 – 153.
- [7] C. COIMBRA, *Mechanics with variable-order differential operators*, Annalen der Physik, 12 (2003), pp. 692–703.
- [8] C. COIMBRA AND R. H. RANGEL, *General solution of the particle momentum equation in unsteady stokes flows*, Journal of Fluid Mechanics, 370 (1998), pp. 53–72.

- [9] I. KIM, S. ELGHOBASHI, AND W. SIRIGNANO, *On the equation for spherical-particle motion: effect of reynolds and acceleration numbers*, Journal of Fluid Mechanics, 367 (1998), pp. 221–253.
- [10] D. KNOLL AND D. KEYES, *Jacobian-free Newton-Krylov methods: a survey of approaches and application*, Journal of Computational Physics, 193 (2004), pp. 357–397.
- [11] M. KOBAYASHI, *On a class of Padé finite volume methods*, Journal of Computational Physics, 156 (1999), pp. 137–180.
- [12] M. KOBAYASHI AND J. M. PEREIRA, *A computational stream function method for two-dimensional incompressible viscous flows*, International Journal for Numerical Methods in Engineering, 62 (2005), pp. 1950–1981.
- [13] S. LELE, *Compact finite difference schemes with spectral-like resolution*, Journal of Computational Physics, 103 (1992), pp. 16–42.
- [14] C. LORENZO AND T. HARTLEY, *Variable Order and Distributed Order fractional operators*, Nonlinear Dynamics, 29 (2002), pp. 57–93.
- [15] M. MAXEY AND J. RILEY, *Equation of motion for a small rigid sphere in a nonuniform flow*, Physics of Fluids, 26 (1983), pp. 883–889.
- [16] R. MEI, *Flow due to an oscillating sphere and an expression for unsteady drag on the sphere at finite reynolds number*, Journal of Fluid Mechanics, 270 (1994), pp. 133–174.
- [17] R. MEI AND R. ADRIAN, *Flow past a sphere with an oscillation in the free-stream and unsteady drag at finite reynolds number*, Journal of Fluid Mechanics, 237 (1992), pp. 323–341.

- [18] R. MEI, C. LAWRENCE, AND R. ADRIAN, *Unsteady drag on a sphere at finite reynolds number with small fluctuations in the free-stream velocity.*, Journal of Fluid Mechanics, 233 (1991), pp. 613–631.
- [19] F. ODAR AND W. HAMILTON, *Forces on a sphere accelerating in a viscous fluid*, Journal of Fluid Mechanics, 18 (1964), pp. 302–314.
- [20] C. W. OSEEN, *Hydrodynamik*, Leipzig: Akademische Verlagsgesellschaft, 1927.
- [21] J. M. PEREIRA AND J. C. PEREIRA, *Fourier analysis of several finite-difference schemes for the one-dimensional unsteady convectiondiffusion equation*, International Journal for Numerical Methods in Fluids, 36 (2001), pp. 417–439.
- [22] I. PODLUBNY, *Fractional Differential Equations*, Academic Press, 1999.
- [23] Y. SAAD, *A flexible inner-outer preconditioned GMRES algorithm*, SIAM Journal on Scientific and Statistical Computing, 14 (1993), pp. 461–469.
- [24] L. SCHILLER AND A. NAUMAN, *A drag coefficient correlation*, VDI Zeitung, 77 (1935), pp. 318–320.
- [25] C. SOON, C. COIMBRA, AND M. KOBAYASHI, *The variable viscoelasticity oscillator*, Annalen der Physik, 14 (2005), pp. 378–389.
- [26] G. G. STOKES, *On the effect of internal friction of fluids on the motion of pendulums*, Transactions of the Cambridge Philosophical Society, III (1850), pp. 8–106.